European Journal of Medicinal Chemistry 312 (2026) 118852

Contents lists available at ScienceDirect

European Journal of Medicinal Chemistry

journal homepage: www.elsevier.com/locate/ejmech

Research paper

Structure-based virtual screening, *in vitro* and *in silico* analysis identified novel potent m6A demethylase FTO inhibitors as promising neurotherapeutic agents

Alba Irisarri [a,b], Aina Bellver-Sanchis [a,b], Bhanwar Singh Choudhary [c], Ana Mallo-Abreu [d,e], Luis Labrador [f], Gemma Casadesus [f], Belén Pérez [g], Abhisek Jana [h], Deb Ranjan Banerjee [h], Isabel Iriepa [i,j], M. Isabel Loza [k,l], José Brea [k,l], Cristina Val [k,l], Mercè Pallàs [a,b,m], Diego Muñoz-Torrero [d,e,*], Christian Griñán-Ferré [a,b,m,**]

[a] Department of Pharmacology, Toxicology and Therapeutic Chemistry, University of Barcelona, Av. Joan XXIII, 27-31, Barcelona, Spain
[b] Institute of Neurosciences of the University of Barcelona, University of Barcelona, Barcelona, Spain
[c] Department of Pharmacy, Central University of Rajasthan, Bandarsindari, Ajmer, India
[d] Laboratory of Medicinal Chemistry, Faculty of Pharmacy and Food Sciences, University of Barcelona, Av. Joan XXIII, 27-31, Barcelona, Spain
[e] Institute of Biomedicine (IBUB), University of Barcelona, Av. Diagonal 643, Barcelona, Spain
[f] Department of Pharmacology and Therapeutics, Health Science Center-University of Florida, Gainesville, FL, USA
[g] Department of Pharmacology, Therapeutic and Toxicology, Universitat Autònoma de Barcelona, Barcelona, Spain
[h] Department of Chemistry, National Institute of Technology Durgapur, Durgapur, India
[i] Universidad de Alcalá, Departamento de Química Orgánica y Química Inorgánica, Instituto de Investigación Química "Andrés M. del Río" (IQAR), Alcalá de Henares, Madrid, 28805, Spain
[j] Grupo DISCOBAC, Instituto de Investigación Sanitaria de Castilla-La Mancha (IDISCAM), Alcalá de Henares, Madrid, 28805, Spain
[k] Innopharma Drug Screening and Pharmacogenomics Platform, Center for Research in Molecular Medicine and Chronic Diseases (CiMUS), Department of Pharmacology, Pharmacy and Pharmaceutical Technology, University of Santiago de Compostela, Santiago de Compostela, Spain
[l] Health Research Institute of Santiago de Compostela (IDIS), University Hospital of Santiago de Compostela (SERGAS), Trav. Choupana s/n, Santiago de Compostela, 15706, Spain
[m] Centro de Investigación en Red, Enfermedades Neurodegenerativas (CIBERNED), Instituto de Salud Carlos III, Madrid, Spain

ARTICLE INFO

Keywords:
Epigenetics
m6A
FTO inhibitors
Hit identification
Neurodegeneration
SAMP8

ABSTRACT

Dysregulation of the m6A RNA demethylase FTO has been implicated in neurodegeneration, but brain-penetrant, selective inhibitors remain scarce. Here, we used structure-based virtual screening of a CNS-oriented library to identify novel FTO inhibitors and characterized their permeability, selectivity, and pharmacological profiles. Among them, compound **VI** showed low-micromolar inhibition of human FTO, selectivity over ALKBH5, high PAMPA-BBB permeability, and oral exposure with measurable plasma levels, moderate brain penetration, and CSF detectability. Molecular dynamics simulations confirmed stable binding of **VI** within the FTO catalytic pocket, consistent with its enzymatic potency and selectivity. In differentiated SH-SY5Y cells, **VI** protected against $A\beta_{1-42}$-induced toxicity while increasing global m6A levels and dampening pro-inflammatory gene expression. In SAMP8 mice, chronic oral treatment with **VI** (3 mg/kg) ameliorated anxiety-like behavior and rescued hippocampal-dependent spatial and recognition memory, concomitant with increased brain m6A and normalization of synaptic and neuroinflammatory markers. Overall, our findings identify compound **VI** as a selective, brain-penetrant FTO inhibitor with favorable pharmacokinetics and disease-modifying efficacy in a sporadic Alzheimer's disease model, supporting its further development as a neurotherapeutic candidate.

* Corresponding author. Laboratory of Medicinal Chemistry, Faculty of Pharmacy and Food Sciences, University of Barcelona, Av. Joan XXIII, 27-31, Barcelona, Spain.
** Corresponding author. Department of Pharmacology, Toxicology and Therapeutic Chemistry, University of Barcelona, Av. Joan XXIII, 27-31, Barcelona, Spain.
E-mail addresses: dmunoztorrero@ub.edu (D. Muñoz-Torrero), christian.grinan@ub.edu (C. Griñán-Ferré).

https://doi.org/10.1016/j.ejmech.2026.118852
Received 30 March 2026; Accepted 7 April 2026
Available online 9 April 2026
0223-5234/© 2026 The Authors. Published by Elsevier Masson SAS. This is an open access article under the CC BY-NC-ND license (http://creativecommons.org/licenses/by-nc-nd/4.0/).

1. Introduction

Epigenetic regulation involves not only DNA and histones but also RNA modifications, adding an important layer of post-transcriptional gene control. N6-methyladenosine (m6A) is the most prevalent internal modification in eukaryotic messenger RNA, first identified in the 1970s [1]. It is controlled by a dynamic system that comprises "writers" (such as the methyltransferases METTL3 and METTL14), "erasers" (including the demethylases FTO (fat mass and obesity-associated protein) and ALKBH5 (AlkB Homolog 5), and "readers" (YTH-domain proteins). As a reversible process, m6A impacts mRNA stability, translation efficiency, alternative splicing, and nuclear export, thereby influencing differentiation, neuronal plasticity, metabolism, and cancer [2]. The discovery of FTO as the first m6A demethylase in 2011 [3] highlighted the reversible and dynamic nature of RNA methylation, sparked renewed interest in RNA epigenetics, and firmly positioned FTO as a potential therapeutic target.

FTO is a non-heme Fe(II)/2-oxoglutarate (2-OG)-dependent dioxygenase responsible for oxidative demethylation of RNA modifications such as m6A, m1A, and m6Am [4]. Its structure includes a catalytic core with a double-stranded β-helix fold that binds Fe(II) and 2-oxoglutarate cofactors, forming a site suitable for small-molecule inhibitor binding [5]. Abnormal FTO activity has been linked to several diseases, including obesity [6–8], acute myeloid leukemia (AML) [9], glioblastoma (GBM) [10], triple-negative breast cancer, head and neck squamous cell carcinoma (HNSCC) [11], metabolic disorders [12–14], and neuropsychiatric disorders like depression [15,16]. In cancer, FTO overexpression promotes cancer stem cell renewal, enables immune evasion through PD-L1 suppression, and shifts metabolism toward glycolysis [9]. In the brain, FTO is highly expressed in neurons, where its dysregulation impairs dopaminergic signaling, memory, and cognition [17–19]. Altered FTO levels have been involved in the development of neurodegenerative diseases such as Alzheimer's disease (AD) [20–22]. Emerging evidence indicates that FTO upregulation reduces neuronal survival, and small-molecule inhibitors have demonstrated neuroprotective effects in preclinical models of neurodegeneration [13,14,23].

Over the past decade, several FTO inhibitors have been discovered [24]. First-generation FTO inhibitors included rhein, meclofenamic acid (MA), MO-I-500 [25], and R-2HG [23,26]. However, many of these early inhibitors exhibited limited selectivity for FTO relative to the similar demethylase ALKBH5 and other AlkB dioxygenases, along with suboptimal pharmacokinetics, such as poor oral bioavailability, short plasma half-lives, and limited blood-brain barrier (BBB) penetration [14,26,27]. To address these issues, structure-guided design has led to second-generation inhibitors with improved potency and selectivity. Notable examples include FB23 (half-maximal inhibitory concentration (IC_{50}) = 0.06 μM) [28] and FB23-2 (IC_{50} = 2.6 μM) [14,27], which were effective in AML xenograft models [28]. More recently, compounds such as FTO-02 (IC_{50} = 2.2 μM) and FTO-04 (IC_{50} = 3.4 μM) have been shown to inhibit glioblastoma stem cell renewal [27]. In recent studies, eriodyctiol was identified as a potent FTO inhibitor targeting obesity-related metabolic disorders, with good pharmacokinetics and no toxicity in preclinical tests, and it functions through the FTO-FOXO1-G6PC/PCK1 and FTO-FOXO1-Ucp1 pathways [29]. Additionally, FTO inhibition has shown potential to enhance radiotherapy for head and neck squamous cell carcinoma (HNSCC) by impairing homologous recombination and increasing DNA damage, without worsening radiation-induced mucositis [11]. In parallel, recent medicinal chemistry campaigns have delivered highly optimised FTO inhibitors, including FB23-derived analogues with improved antileukaemic properties and fragment-merged chemotypes identified by structure-based design in oncology settings [5,30,31]. Despite these advances, major challenges persist for FTO inhibitors intended for central nervous system (CNS) applications. In particular, there is a pressing need to optimize BBB permeability, tissue selectivity, safety, and pharmacokinetic properties compatible with chronic treatment in neurodegenerative diseases.

In this study, we employed a structure-based virtual screening approach using a large chemical library enriched with drug-like and CNS-active molecules to identify FTO inhibitors with improved pharmacological properties. We performed computational docking at the Fe (II)/2-OG catalytic site, MM-GBSA binding energy analysis, and CNS multiparameter optimization (MPO) scoring to identify promising candidates. The top compounds were then tested experimentally to determine their blood-brain barrier permeability and FTO inhibitory activity using parallel artificial membrane permeation assay (PAMPA)-BBB models and enzymatic demethylation assays, respectively. Cellular activity assays were used to determine their therapeutic potential, and, finally, *in vivo* pharmacokinetic evaluations of selected compounds were performed, compared with the reference FTO inhibitor FB23. Our findings reveal new chemical scaffolds compared to previously reported FTO inhibitors (Fig. 1) with stronger binding to FTO's catalytic cavity and improved brain permeability, providing promising leads for further development as treatments for cancer, metabolic disorders, and neurodegenerative diseases.

2. Methodology

2.1. Structure-based virtual screening

The crystal structure of human FTO in complex with the pyridyl glycinamide derivative MD6 (PDB ID 4IE5) [35] was selected for developing the docking model based on resolution, sequence length, PDB validation, and co-crystallized molecule. Protein refinement was performed using the Protein Preparation Wizard. The active site was defined around the co-crystallized *N*-[(3-hydroxypyridin-2-yl)carbonyl] glycine (MD6) using the receptor grid generation module of Glide [36]. A Chembridge CNS MPO library of 496,644 compounds was downloaded from the Chembridge portal and prepared with *LigPrep* using the OPLS 2005 force field [36]. The prepared Chembridge CNS MPO library was screened using virtual screening workflow docking protocols in the Schrödinger software package on the selected crystal structure (PDB ID: 4IE5), carrying forward 10 % from each step, HTVS (High Throughput Virtual Screening) to SP (Standard Precision virtual screening) and SP to XP (Extra Precision virtual screening) and the top 100 were kept in XP docking [37,38]. The top-scoring 100 molecules in XP docking were subjected to binding affinity (dG) calculations using the Prime-MM-GBSA method [32]. From these top 100 molecules, 12 molecules were selected based on the Glide XP docking score, dG of binding, nature of interaction with FTO active site key residues (electrostatic and hydrogen-bonding interactions with the side chains of Arg316, Ser318, and Tyr295, chelation of the FTO-Zn to the inhibitor through the side chain of His231, Asp233, and His307) [35] and scaffold novelty. Stereoisomers of the selected virtual hits were also docked to analyze and differentiate their interactions at the binding site.

2.2. PAMPA-BBB assay

Brain penetration was assessed using a parallel artificial membrane permeation assay for the blood-brain barrier (PAMPA-BBB), following the method of Di et al. [39]. The *in vitro* brain permeability (P_e) of 14 commercial drugs, using a lipid extract of porcine brain membranes, was determined for the test compounds. Commercial drugs and tested compounds were evaluated using a PBS:EtOH (70:30) mixture. Assay validation was performed by comparing the experimental permeability of the reference drugs with the corresponding values reported in the literature. A linear correlation between the experimental and reported permeabilities of the fourteen commercial drugs was obtained ($y = 1.572x - 1.147$; $R^2 = 0.9452$). Based on this equation and considering the limits established by Di et al. [39]. For BBB permeation, we defined permeability ranges as follows: compounds with high BBB permeation (CNS+): P_e (10^{-6} cm s^{-1}) > 5.14; compounds with low BBB

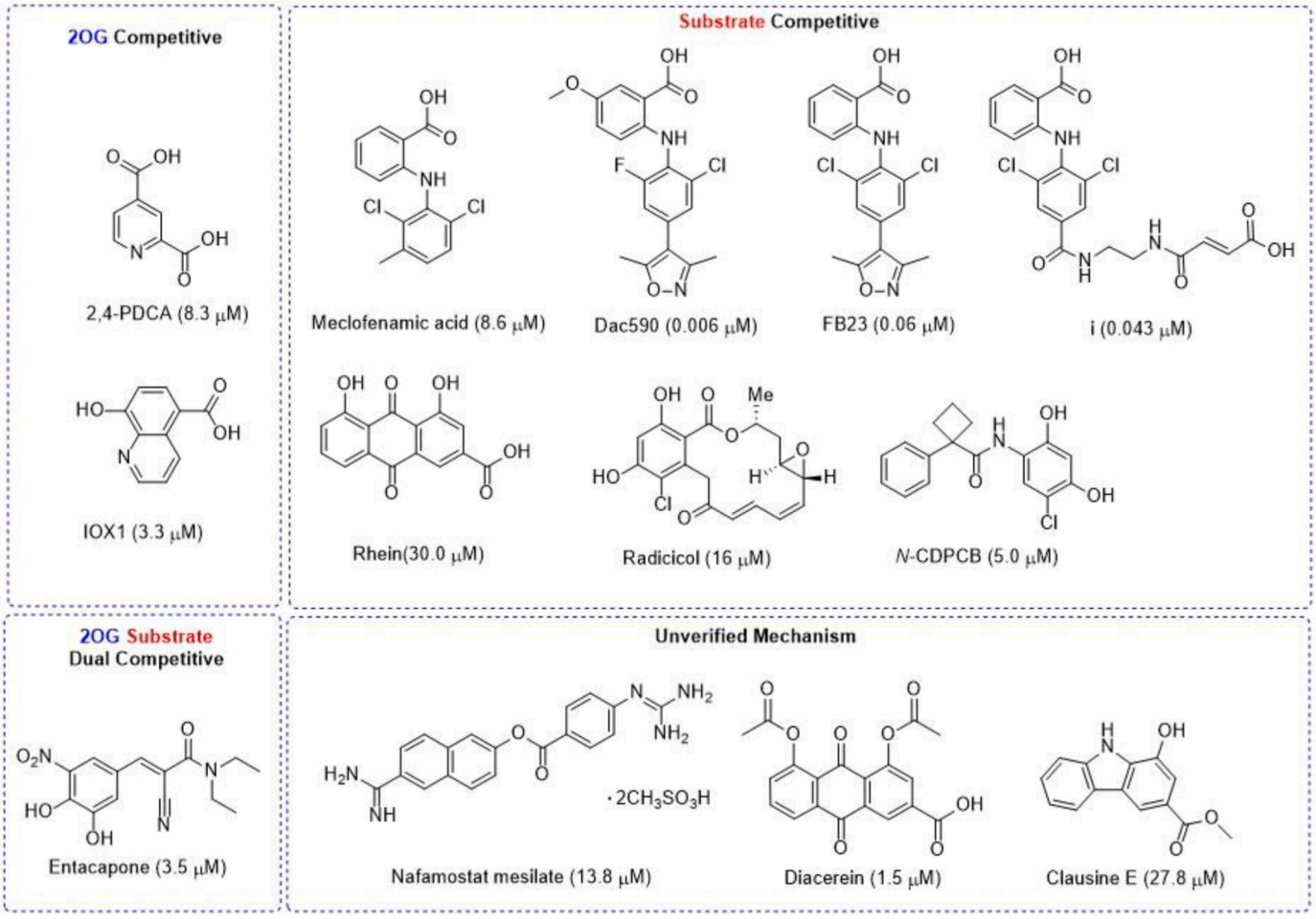


Fig. 1. Chemical structure of previously reported FTO inhibitors. 2-OG competitive FTO inhibitors: 2,4-PDCA, IOX1; substrate competitive FTO inhibitors: Meclofenamic acid, Dac590 [32], FB23 [28], i [33], Rhein, Radicicol, *N*-CDPCB; 2-OG-substrate dual competitive inhibitors: Entacapone; and unverified mechanism: Nafamostat mesilate, Diacerein, Clausine E [34].

permeation (CNS-): P_e (10^{-6} cm s^{-1}) < 1.99; and compounds with uncertain BBB permeation (CNS+/−): 5.14 > P_e (10^{-6} cm s^{-1}) > 1.99.

2.3. Preparation of inhibitor solutions

FTO inhibitors were serially diluted from 5 mM to 0.001 mM in 100% DMSO (Sigma, St. Louis, USA). Then, the respective concentrations were diluted in MilliQ-purified water to reach a final concentration ranging from 50 μM to 0.01 μM in 1 % DMSO in each well.

2.4. FTO chemiluminescence assay kit

Human FTO activity was measured by performing the FTO chemiluminescence assay kit (Catalog #79344, BPS Bioscience, San Diego, CA, USA). 5 μL of different FTO inhibitors was added to a 96-well strip plate precoated with methylated FTO substrate (m^6A). 25 μL of master mix was added, and the reaction was initiated by adding 20 μL of diluted human FTO enzyme. The reaction was incubated overnight at room temperature (RT) with slow shaking. The strip plate was washed three times with 200 μL of 0.1% TBS-T (Tris-buffered saline containing 0.05% Tween 20). 100 μL of blocking buffer was added to each well, and the plate was incubated at RT with shaking for 10 min. The supernatant was removed, and 100 μL of a 100-fold-diluted primary antibody was added to each well. The strip plate was incubated at RT for 1 h with slow shaking. The plate was washed three times with 200 μL of TBST buffer. 100 μL of blocking buffer was added to each well, and the plate was incubated at RT with shaking for 10 min. 100 μL of a 1000-fold-diluted secondary HRP-labeled antibody was added to each well, and the plate was incubated at RT with slow shaking for 30 min. The strip plate was washed three times with 200 μL of TBST buffer. Finally, 100 μL of substrate mix (ELISA ECL Substrate A and ELISA ECL Substrate B) was added, and the luminescence was measured with an integration time of 1 s in a TECAN Infinite® 200 PRO plate reader. All reagents used are described in the manufacturer's protocol.

2.5. ALKBH5 chemiluminescence assay kit

Human ALKBH5 activity was measured by performing an ALKBH5 chemiluminescence assay kit (Catalog #79659, BPS Bioscience, San Diego, CA, USA) using the same procedure described above for the determination of the FTO inhibitory activity.

2.6. Dataset preparation and 3D-QSAR pharmacophore generation

To prepare the machine-learning dataset for 3D-QSAR pharmacophore generation, 33 reported FTO inhibitors were selected. These inhibitors were further divided into (i) a training set of a total of twenty compounds, and (ii) a test set of a total of thirteen compounds. The training set compounds were fed directly into the machine learning algorithm to generate the 3D QSAR pharmacophore model; therefore, their activity span was chosen to cover four orders of magnitude based on their reported IC_{50} values (from 70 nM to 59.600 nM) to ensure

statistical significance. On the other hand, the test set compounds were used to validate the generated pharmacophore. Based on the IC_{50} values of all the compounds, both training set and test set compounds were divided into four groups, namely: highly active ($IC_{50} \leq 2$ μM, +++); moderately active (2 μM < $IC_{50} \leq 10$ μM, ++), and inactive ($IC_{50} > 10$ μM, +). ChemDraw Ultra 12.0 was used to generate 2D structures, followed by conversion to 3D structures using BIOVIA Discovery Studio (DS) Academic Research Suite (BIOVIA, 2022), Dassault Systèmes, BIOVIA Discovery Studio Academic Research Suite, San Diego: Dassault Systèmes, (n.d.). For the energy minimization of all the training and test sets of compounds, the CHARMm force field [40] was employed to generate the highest number of 255 conformations for each using the BEST conformational algorithm (BIOVIA, 2022), Dassault Systèmes, BIOVIA Discovery Studio Academic Research Suite, San Diego: Dassault Systèmes, (n.d.). Only the lowest-energy conformations of the training and test compounds were used for pharmacophore generation and validation, respectively. The 3D QSAR pharmacophore models were built from the chemical features of the most and least active compounds in the training dataset. Purposefully, the AI-ML-embedded HypoGen algorithm in BIOVIA Discovery Studio was used to build and rank pharmacophores from the training set compounds based on chemical features and activities (IC_{50}). In this ML approach, the HypoGen algorithm correlates the reported activities with the estimated activities as estimated based on the geometric fit and identification of complementary pharmacophore features such as hydrogen bond donor (HBD), hydrogen bond acceptor (HBA), hydrophobic (HYP), positive ionizable (PI), and aromatic ring (AR). The uncertainty factor was set to 2.0, the minimum inter-feature distance to 1.0 Å, and the maximum and minimum numbers of features to 5 and 1, respectively, to generate the 3D QSAR pharmacophore. All other parameters were kept at their default values. A total of 10 pharmacophores were generated using different statistical parameters, including root mean square (RMS) deviation, cost, maximum fit, and correlation values. The ten generated hypotheses were validated using internal methods (cost analysis, Fisher's Randomization method) and an external method (test dataset).

2.7. Molecular dynamics simulations

Molecular dynamics (MD) simulations help understand microscopic events, such as ligand binding and associated macromolecular movements, that occur in computationally simulated environments. Here, we have performed MD simulations of the 5 FTO-inhibitors and their stereoisomers in complex with human FTO (4IE5-**(*S*)–I**, **(R)-I**, **(*S*)–V, (*R*)-V**, **(*S*)-VI (*R*)-VI**, **VII**, and **X**, Fig. 2), using the *Desmond* module of Maestro 2025-2 (Version 14.4). Full-atom MD simulations were performed for all protein-ligand complexes using *Desmond* 2025-2 (Maestro, version 14.4) [41] in three steps: system builder, minimization, and MD simulation. A simple point-charge (SPC) solvent model with an orthorhombic boundary box was used to build the model. The system was further neutralized by adding a calculated amount of Na^+ and 0.15 M NaCl. The system was subjected to energy minimization for 100 ps to rule out steric clashes. 500 ns simulations were performed post-equilibration of the complex system, using the constant-temperature constant-pressure (NPT) ensemble at 300 K and 1 bar for all 5 FTO-inhibitor protein-ligand complexes. The MD trajectory analysis, protein RMSD (Root Mean Square Deviation), protein RMSF (Root Mean Square Fluctuation), and ligand RMSF were calculated after the MD simulations using md-out.cms file. MM-GBSA-based ΔG calculation was performed using the thermal_mmgbsa.py script for each frame of the MD trajectory using Maestro 14.3 [42]. Using the average ΔG of all frames of MD trajectories lnK (natural logarithm of the equilibrium constant K) was calculated using Gibbs free energy and the equilibrium constants equation:

$$lnK = \frac{\Delta G}{-R}$$

Here, lnK is the natural logarithm of the equilibrium constant K, ΔG is the calculated average MMGBSA dG bind, R is the gas constant with a value of 0.008314 J mol^{-1} at T, the temperature of the reaction in Kelvin, which is 300 K here.

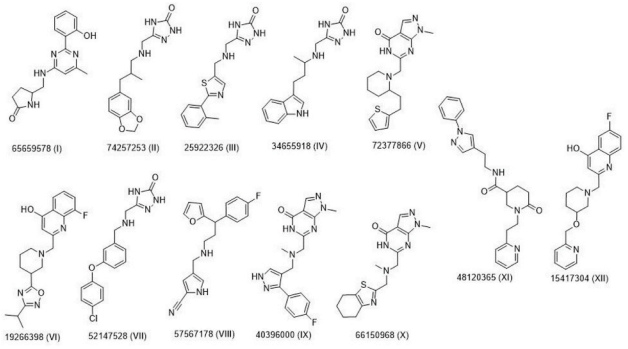


Fig. 2. Chemical structure of the selected FTO inhibitor virtual hits.

2.8. SH-SY5Y differentiation

To induce cell differentiation, SH-SY5Y cells were treated with 10 μM retinoic acid (RA). First, cells were seeded onto 24-well plates (Catalog #3524, Costar®, Corning, USA) at approximately 40% confluency. Day 1 cells were maintained in basic growth medium consisting of Opti-MEM (Catalog #31985070, Gibco Life Technologies, Thermo Fisher Scientific, USA) supplemented with 10% heat-inactivated fetal bovine serum (hiFBS) and 1 × penicillin/streptomycin (Catalog #10082147 and #15140122, Gibco Life Technologies, Thermo Fisher Scientific, USA). The following day, the medium was replaced with another medium composed of`Dulbecco's modified Eagle's medium (DMEM) (Catalog #SH30081.FS, CYTIVA, USA) supplemented with 5% hiFBS, 1 × penicillin/streptomycin (P/S), and 10 μM RA. The medium was refreshed after two days. On day 7, differentiation was considered complete, and the medium was replaced with serum-free medium for 24 h before subsequent treatments.

2.9. Neuroprotection assay and cytotoxicity evaluation

For neuroprotection assays, differentiated cells were first pre-incubated for 30 min with the FTO inhibitors or the corresponding vehicle control. The medium was then replaced with fresh serum-free medium containing β-amyloid (Aβ) (1-42) (Catalog #HY-P1363, MedChemExpress, USA) (5 μM) together with the same concentration of inhibitor or vehicle, and cells were further incubated for 24 h before lactate dehydrogenase (LDH) activity measurements. Control cells received vehicle alone and were not exposed to Aβ or inhibitors, whereas an Aβ-only group was treated with Aβ (1-42) (5 μM) in the absence of inhibitors to define the baseline toxicity. A positive control for maximal cell death was obtained by treating cells with Triton X-100 (Catalog #9002-93-1, Sigma-Aldrich, USA) (4%) for 30 min before LDH quantification.

Quantification of cell death and cell lysis was performed by the measurement of LDH activity released from the cytosol of damaged cells into the supernatant (Roche diagnostics, following manufacturer's protocol).

2.10. hERG inhibition assay

The assay was carried out at a CHO cell line transfected with the hERG potassium channel. 72 h before the assay, 2500 cells were seeded on a 384 well black plate (Catalog #781091 Greiner, Spain). Cell lines were maintained at 37 °C in a 5% CO_2 atmosphere for 24 h and at 30 °C in a 5% CO_2 atmosphere for 48 h plus. hERG activity was measured by

using the Fluxor™ Potassium Ion Chanel Assay Kit (Catalog #F10016, Thermo Fisher Scientific, USA). Medium was replaced with 20 µl Loading Buffer and the cells were incubated for 60 min at RT, protected from direct light. After incubation, Loading Buffer was replaced for Assay buffer and the compounds were incubated for 30 min at RT. 5 µl of Stimulus Buffer was added to each well and the fluorescence was read ($\lambda ex = 490$ nm, $\lambda em = 525$ nm) using imaging plate reader system (Catalog #FDSS7000EX, Hamamatsu, Japan) every second after the establishment of a baseline line.

2.11. Plasma stability assay

The methodology involved adjusting the plasma pH to 7.4 prior to the assay. Compounds were then added to the plasma at a final concentration of 5 µM in a total volume of 500 µL per well. Plates were incubated at 37 °C with 0.5% CO_2, and aliquots were collected at 0, 60, 120, and 360 min. For protein precipitation, 300 µL of acetonitrile was added to each aliquot, followed by centrifugation at 4,000 g for 15 min at 4 °C. The clear supernatant was carefully transferred to a clean plate and analyzed by UPLC/MS/MS for sample quantification, using an ACQUITY BEH C18 column (1.7 µm, 2.1 × 100 mm, Waters) as the stationary phase and a mobile phase consisting of 0.1% formic acid in water/0.1% formic acid in acetonitrile (Table 1).

The chromatographic equipment employed was an UPLC QSM Waters Acquity/XevoTQD. Compound concentrations were calculated from the MS peak areas.

2.12. Solubility assay

A 10 mM stock solution of the compound was serially diluted to decreased molarity, from 300 µM to 0.1 µM, in 384 well transparent plate (Catalog #781801, Greiner, Spain) with 1% DMSO: 99% DPBS buffer (Catalog #D8537, Sigma-Aldrich Steinheim, Germany). The plate was incubated at 37 °C for 2 h and the light scattering was measured in a Nephelostar Plus reader (BMG LABTECH). The results were adjusted to a segmented regression to obtain the maximum concentration in which compounds are soluble.

2.13. Pharmacokinetic studies

The *in vivo* pharmacokinetic (PK) study was conducted in 60 female CD1 mice weighing approximately 30 g (n = 3 per group). Animals were randomized to the treated or control groups. A single intraperitoneal dose of 3 mg/kg was administered to FB23 and compound **VII** groups. In the case of compound **VI**, the administration was performed by oral gavage at the same dose. The compounds were dissolved in vehicle (Catalog #D4540, 1% DMSO, Sigma-Aldrich, Steinheim, Germany) with 20% w/v of 2-hydroxypropyl-β-cyclodextrin (Catalog #AT-20762, Atomole Scientific Co. Ltd., Wuhan, Hubei, China). Mice were monitored for signs of pain or distress during the time between injection and euthanasia. Mice were sacrificed by cervical dislocation and blood was collected at different time points (0 min, 5 min, 15 min, 30 min, 60 min, 120 min, 240 min, 360 min, 1440 min after injection for FB23 and **VII**; and, 0 min, 5 min, 15 min, 45 min, 90 min, 120 min, 240 min, 480 min, 1440 min after injection for **VI**) in microtubes with serum gel and clotting activator (Catalog #NC9436363, Sarstedt Inc Push Cap Micro Tube, 1.1 mL, Serum-Gel), followed by a collection of the brain. Brain tissue was frozen in dry ice powder and stored at − 80 °C until use. Blood samples were centrifuged at 10,000 rpm for 10 min at 4 °C to obtain plasma. Bioanalysis of analyte concentration was performed by LC-MS/MS method and PK analysis using Phoenix WinNonlin® software version 8.3.

2.14. Animals

5-month-old SAMR1 (n = 4) and SAMP8 mice (n = 8) were used for behavioral studies. Animals had free access to food and water and were maintained under standard temperature conditions (22 ± 2 °C), controlled humidity, and a 12-h light/dark cycle (300 lx/0 lx). SAMP8 mice were randomized into SAMP8 Control (n = 4) and SAMP8 **VI** (3 mg/kg) (n = 4). Animals were weighed daily. Experimental groups received either a daily dose of vehicle (Catalog #D4540, 1% DMSO, Sigma-Aldrich, Steinheim, Germany) with 20% w/v 2-hydroxypropyl-β-cyclodextrin (Catalog #AT-20762, Atomole Scientific Co. Ltd., Wuhan, Hubei, China) or 3 mg/kg per day of compound **VI** dissolved in vehicle via oral gavage during the treatment period. After 4 weeks of treatment, behavioral and cognitive tests were performed. During this period and until sacrifice, mice were treated either with vehicle or compound **VI**.

2.15. Open field test (OFT)

The OFT was performed to assess the emotional changes and anxiety-like behavior of the mice. A white polywood apparatus (50 × 50 × 25 cm) was used for the test. The bottom of the apparatus was divided into a central and a peripheral area (15 cm between the central area and the wall). Mice were placed in the center of the open field arena and allowed to explore the apparatus for 10 min. After the session, the mice were returned to their home cages, and the open field was cleaned with 70% ethanol and dried between sessions. Parameters assessed included time spent in the central and peripheral zones, number of rearing, grooming, defecation, and urination.

2.16. Object location test (OLT)

The OLT was performed to investigate mice's spatial memory when exposed to a new location of an already known object. This test is based on the spontaneous tendency of mice to spend more time exploring a novel location rather than a known one and to recognize when an object has been misplaced. The test was performed in a wooden box (50 × 50 × 25 cm), with three white walls and the last black. On the first day, the animals were habituated to the empty outdoor area for 10 min. On the second day, two identical objects were placed in front of the black wall, equidistant from each other and from the wall. The objects were 10 cm high. The animals were brought into the open field arena and allowed to explore the objects and the surroundings for 10 min. The animals were then returned to their home cages, and the OLT apparatus was cleaned with 70% ethanol. After 24 h, an object was relocated in front of the opposite white wall to assess spatial performance of the mice. Trials were recorded with a camera placed above the open field area, and the total exploration time was determined by counting the time (in seconds) spent sniffing the object at the new location (TN) and the object at the old location (TO). The discrimination index (DI), which is define– as (TN − TO)/(TN + TO), was calculated to assess the cognitive performance.

2.17. Novel object recognition test (NORT)

Short- and long-term memory was analyzed by NORT. The test was performed in a 90°, two-armed, 25-cm-long, and 20-cm-high black maze. The light intensity in the middle of the field was 30 lx. The objects to be discriminated were plastic figures (object A, 5.25 cm high; and object B, 4.75 cm high). The mice were acclimatized to the device for 10 min on 3 consecutive days (habituation phase). On day 4, they performed a 10-min acquisition trial (familiarization phase) in which they were placed in the maze and allowed to explore two identical novel objects (A + A or B + B) at the end of each arm. Objects A and B were counterbalanced to avoid a bias in object preference so that half of the animals in each experimental group were first confronted with object A and the other half with object B. For the analysis of long-term memory, object C was used as the novel object for both groups. The 10-min retention trials (test phase) took place 2 h (short-term; A + B or B +

A) and 24 h (long-term; A + C or B + C) after the habituation phase. During the test phase, one of the two identical objects was replaced by a novel one and the time spent exploring the new object (TN) and the old object (TO) was measured manually. The discrimination index (DI) was calculate– as (TN − TO/TN + TO). Sniffing or touching objects with the nose and forepaws was considered exploration. The maze, surface and objects were cleaned with 70% ethanol between trials to eliminate olfactory cues.

All procedures involving animals and dissection and removal of brains, followed ARRIVE and the standard ethical guidelines (Council of the European Communities Directive 2010/63/EU and Guidelines for the Care and Use of Mammals in Neuroscience and Behavioral Research, National Research Council 2003) and were approved by the Institutional Animal Care and Generalitat de Catalunya (#10291, January 28, 2018). Every effort was made to minimize the number of mice used and their suffering.

2.18. Isolation of the tissues

Neuron cells were harvested by scraping. Culture medium was removed, and cells were washed with PBS 1X for further scraping into TRItidy G™ reagent (Catalog #A4051ITW, Reagents, Panreac AppliChem). Recollected cells were stored at − 80 °C until use.

The mice were euthanized by cervical dislocation 3 days after the last experiment was performed. The hippocampus and cortex were quickly dissected from the brain. All tissues were frozen in dry ice powder and stored at − 80 °C until use.

2.19. RNA extraction and determination of gene expression

Isolation of total RNA from cells (n = 3 per group) and brain samples (n = 4 mice per group) was performed using TRItidy G™ reagent (Catalog #A4051ITW, Reagents, Panreac AppliChem) according to the manufacturer's instructions. Reverse transcription polymerase chain reaction (RT-PCR) was then performed as follows: 2 μg of messenger RNA (mRNA) was reverse transcribed using the High-Capacity cDNA Reverse Transcription Kit (Catalog #4368813, Applied Biosystems™, Vilnius, Lithuania). qPCR was performed with the StepOnePlus™ Real-Time PCR System (Catalog #4376600, Applied Biosystems™, Vilnius, Lithuania), using the SYBR Green PCR Master Mix (Catalog #K0253, Applied Biosystems™, Vilnius, Lithuania). Briefly, each reaction mixture consisted of 6.75 μL of cDNA (at a concentration of 2 μg), 0.75 μL of each primer (at a concentration of 100 nM), and 6.75 μL of SYBR Green PCR Master Mix (2X). The primer sequences are listed in Table S1 and Table S2. For all the studies, RNA yield, purity, and quality were determined using a NanoDrop™ ND-1000 (Thermo Fisher Scientific, Waltham, MA, USA). Samples were also tested in an Agilent 2100B Bioanalyzer (Agilent Technologies, Santa Clara, CA, USA) to determine the RNA integrity. RNAs with a 260/280 ratio number of 1.8-2 and a RIN number of 7.5, respectively, were selected. The comparative cycle threshold (Ct) (ΔΔCt) method was used to analyze the data, using the housekeeping gene β-actin level to normalize for differences in sample loading and preparation. Each sample was analyzed in duplicate, and the results represented the n-fold difference in transcript levels between the different groups.

2.20. Quantification of m6A RNA methylation

Total RNA extraction from cells (n = 3 per group) and brain tissue (n = 4 mice per group) was performed using TRItidy G™ reagent, and RNA yield, purity, and quality were determined, as described in the previous section. Quantification of m6A RNA methylation was performed using the EpiQuik™ m6A RNA Methylation Quantification Kit (Colorimetric) (Catalog #P-9005, Epigentek), according to the manufacturer's protocol. 200 ng of RNA of each sample were loaded to the plate, and the absorbance was measured at 450 nm in a microplate spectrophotometer (Varioskan LUX, Thermo Fisher Scientific, USA). The optical density was considered proportional to the amount of m6A.

2.21. Statistical analysis

Data analysis was conducted using GraphPad Prism ver. 9 statistical software. For IC_{50} calculation, non-linear regression was performed. Values are shown as the mean ± standard deviation (SD) of at least two replicates. For ALKBH5 inhibition percentage calculation, negative values were considered as a mean of zero ± standard deviation (SD) of at least two replicates. For cell survival analysis, behavioral studies, and molecular m6A and gene expression determination, means were compared using one-way ANOVA followed by Dunnett's post hoc analysis. Results were expressed as mean ± standard error of the mean (SEM). Statistical significance was assumed when p-values were <0.05. Statistical outliers were identified using Grubbs' test and removed from the analysis. A blind analysis was performed for the behavioral tests.

3. Results and discussion

3.1. Identification of novel FTO inhibitors through structure-based virtual screening

A hierarchical stepwise virtual screening was performed using Glide HTVS, SP, and XP docking for the Chembridge database of 496,644 compounds. The top 100 compounds were selected, based on docking scores from the CNS MPO database of Chembridge Corporation, for further analysis. The docking scores of the top 100 compounds ranged from −13.9 to −8.5. The Molecular Mechanics-Generalized Born Surface Area (MM-GBSA) dG binding affinity of these 100 compounds ranged from −102.5 kcal/mol to −46.4 kcal/mol 12 molecules were selected based on the Glide XP dock score, MM-GBSA dG binding affinity, hydrogen bond mediated interaction with FTO active site residues (Fig. 2), i. e. electrostatic and hydrogen-bonding interactions with the side chains of Arg316, Ser318, and Tyr295, chelation of the FTO-Zn to the inhibitor through the side chains of His231, Asp233, and His307, and scaffold novelty. These selected molecules were further screened with the Pan-assay Interference Compounds (PAINS) filter, and all were found to be non-PAINS.

3.2. In vitro BBB penetration study

PAMPA-BBB evaluation was performed for the well-established reference FTO inhibitor FB23 [28] and the 12 selected compounds, to assess the desired CNS permeation (see Table 2). FB23 showed a poor *in vitro* BBB permeability (P_e) of $4.3 \times 10^{-6} \pm 0.2$ cm · s^{-1} (Table 2), with this result (CNS+/−) being indicative of a likely compromised ability to penetrate the CNS. Like FB23, compounds **IV** and **XII** also showed uncertain BBB permeation, and compounds **III**, **IX**, and **XI** showed a low BBB permeability (CNS-). Gratifyingly, 6 out of the 12 hits, namely compounds **I**, **V**, **VI**, **VII**, **VIII**, and **X** had P_e values much higher than that of the reference inhibitor FB23 and clearly above the threshold for high BBB permeation ($P_e > 5.14 \times 10^{-6}$ · s^{-1}), with permeabilities in the range 12.2 to 28.4×10^{-6} · s^{-1} (Table 2, Table S3). Thus, these compounds are expected to be able to cross the BBB and interact with their

Table 1
Mobile phase gradient.

Time (min)	Water	Acetonitrile
0	100%	0%
0.1	100%	0%
1	0%	100%
2	0%	100%
2.1	100%	0%
2.5	100%	0%

Flow: 0.6 ml/min.

Table 2
Permeability (P_e 10^{-6} cm s^{-1}) in the PAMPA-BBB assay and predictive penetration in the CNS of the FTO inhibitor hits and the reference inhibitor FB23.

Compound	Experimental value (n = 3) ± S.D.	CNS Prediction
FB23	4.3 ± 0.2	CNS ±
I	14.6 ± 1.0	CNS+
II	5.6 ± 0.2	CNS ±
III	1.5 ± 0.1	CNS-
IV	3.0 ± 0.3	CNS ±
V	28.4 ± 1.0	CNS+
VI	12.2 ± 1.1	CNS+
VII	15.3 ± 1.2	CNS+
VIII	18.4 ± 1.1	CNS+
IX	0.3 ± 0.05	CNS-
X	21.3 ± 1.5	CNS+
XI	1.2 ± 0.2	CNS-
XII	3.2 ± 1.2	CNS ±

biological targets in the CNS, thereby constituting promising tools for *in vivo* studies. Moreover, these positive results highlight that combining structure-based virtual screening with CNS MPO [43] filtering effectively identifies compounds with favorable brain penetration, overcoming a key challenge of first-generation FTO inhibitors.

3.3. In vitro determination of FTO inhibition activity

The percentages of inhibition of human FTO activity by the 6 selected brain-permeable hits were determined using the m^6A substrate, and IC_{50} values were calculated. As a control, we used the reference FTO inhibitor FB23. With the sole exception of compound **VIII**, which was found inactive, the other 5 hits displayed 1–2-digit micromolar IC_{50}s (Table 3). Among them, compound **VI** was the most potent, with a single-digit IC_{50} (1.1 μM), only 9-fold less potent than the reference FB23.

3.4. In vitro selectivity over ALKBH5 inhibition

The percentage inhibition of the activity of ALKBH5 of the 5 selected compounds that were found to be brain-permeable and active against human FTO was determined at 10 μM, using substrate m^6A, to discriminate the selectivity for FTO over ALKBH5 enzymes. FB23 was used as a control, as it showed no inhibition of ALKBH5 (0.0 ± 2.4). Compounds **I**, **V**, and **X** showed partial inhibition of ALKBH5 (35.0 ± 0.2 μM, 38.0 ± 0.9 μM, and 15.4 ± 0.2 μM, respectively; Table 4), although none exceeded 40%. In contrast, compounds **VI** and **VII** showed no inhibition of ALKBH5 at 10 μM, thereby being fully selective for FTO over ALKBH5 inhibition, like the reference FTO inhibitor FB23.

3.5. 3D-QSAR mapping of selected hits

We built the 3D QSAR pharmacophore against FTO enzyme-based Training Dataset and validated the model based on Test Dataset using AI/ML-embedded program of commercially purchased BIOVIA Discovery Studio academic research suite as depicted in Fig. 3.

Table 3
IC_{50} values of the selected brain-permeable hit compounds and the reference inhibitor FB23.

Compound	IC_{50} ± SD (μM)
FB23	0.1 ± 0.02
I	41.4 ± 2.2
V	66.3 ± 0.5
VI	1.1 ± 0.1
VII	5.9 ± 0.4
VIII	No inhibition
X	17.7 ± 0.9

Table 4
Inhibition of ALKBH5 activity was determined at a fixed inhibitor concentration of 10 μM.

Compound	Average % inhibition ±SD
FB23	0.0 ± 2.4
I	35.0 ± 0.2
V	38.1 ± 0.9
VI	0.0 ± 0.3
VII	0.0 ± 0.9
X	15.4 ± 0.2

In short, 20 known FTO inhibitors with wide-ranging activities, in the range 0.07-59.6 μM, were selected as the Training dataset for machine learning-based 3D QSAR building (Fig. S1). The hypothesis generated was analyzed using statistical parameters (cost, correlation, and error; see Table S4), and the pharmacophore Hypo1 was selected as the best hypothesis for the next step (Table S5). Subsequently, Hypo1 was analyzed to map the chemical features and intra-feature spatial distances for H-bond acceptor (green), H-bond donor (pink), hydrophobic (cyan), and ring aromatic (orange) within a restricted spatial orientation (Fig. S2). Then, Hypo1 was fitted to the most active and least active inhibitors in the training set (Fig. S2) to achieve satisfactory internal validation. The Hypo1 was further subjected to external validation against a Test dataset having twelve FTO inhibitors via (i) Correlation graph having predicted vs. experimental activities, (ii) Fischer's randomization method (Table S6, Fig. S3).

After satisfactory internal and external validation, Hypo1 was mapped against the reference FB23, and the 5 selected hits with experimentally confirmed brain permeability and human FTO inhibitory activity (**I**, **V**, **VI**, **VII**, **X**) were used to gain molecular-level insights into their inhibitory potencies (Fig. 3). The mapping of the inhibitors into Hypo1 was performed using the embedded program in BIOVIA Discovery Studio. The program elucidates the fitting and three-dimensional positions of the candidates within the complementary features of Hypo1 and ranks them based on the fitting parameters and their predicted IC_{50} values. The mapping of the FB23 into the 3D-QSAR pharmacophore Hypo1 depicts complementary intra-feature mapping of the reference within the restricted spatial arrangements. The benzoic acid moiety of FB23 perfectly fits into the H-bond acceptor (green) and hydrophobic (cyan) features of the Hypo1; the –NH of FB23 fits into the H-bond donor feature (pink), and the heterocyclic ring perfectly positions into the ring aromatic feature (orange) of the Hypo1. Thus, the FB23 mapping with a good fit value predicts an IC_{50} of 0.08 μM, which is very close to the experimental value (0.13 μM). Likewise, we carried out the mapping of the selected inhibitors (**I**, **V**, **VI**, **VII**, **X**) into the 3D-QSAR pharmacophore Hypo1 noticing the fitting of the chemical features of the compounds into the pharmacophoric features mostly, leading to the ranking in fitting value and corresponding estimated IC_{50} within an acceptable Pearson's correlation error value (R = 0.86) range with the experimental IC_{50} of these inhibitors (Fig. 3).

3.6. Molecular modelling and MD simulations

Molecular modelling and MD simulation studies, followed by MM-GBSA-based calculation of the natural logarithm of the binding equilibrium constant for comparative binding affinity analysis, were carried out for the *R* and *S* stereoisomers of **I**, **V**, and **VI** to assess binding modes and correlate them with the probable higher-activity isomer. The pyrimidine moiety of **(*R*)-I** is inclined towards His231 and Arg322 and interacts through H-bond acceptor interaction, but in the case of **(*S*)–I**, the pyrimidine moiety slightly shifts away from Arg322 and loses the H-bond interaction with it (Fig. S4A and B). The same is reflected in the RMSD plot from MD simulations, where **(*R*)-I** remains comparatively more stable than **(*S*)–I** (Fig. S5C and D). Also, the (*R*)-isomer has approximately 6 times higher binding affinity than the (*S*) enantiomer (Table 5). In the case of **(*R*)-V** and **(*S*)–V** enantiomers, the orientation of

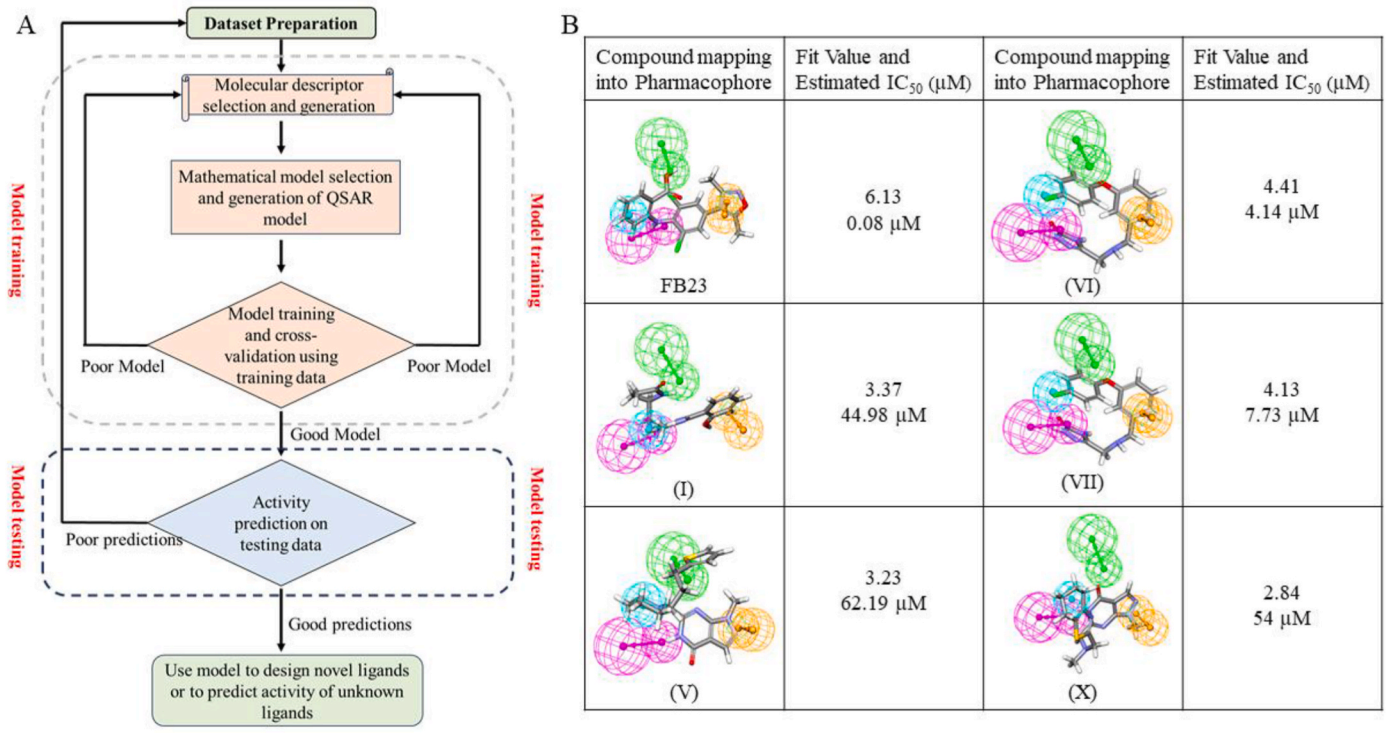


Fig. 3. (**A**) Schematic Representation of AI-ML embedded 3D-QSAR pharmacophore generation method against FTO enzyme inhibitors; (**B**) Mapping of the reference and the five selected inhibitors, with experimentally demonstrated BBB permeability and FTO inhibitory activity, into the validated 3D-QSAR pharmacophore Hypo1. The machine learning approach provides an estimated activity based on the spatial and geometric fitting of the compounds to complementary pharmacophore features. In our case, the estimated activities of the reference FB23 and the five selected inhibitors correlate perfectly with the experimental activities, with a minimal error.

Table 5
Average binding energy (ΔG) of all MD trajectories and equilibrium constant of FTO inhibitors.

FTO inhibitor	Average ΔG (Kcal/mol)	lnK
FB23	−45.0 ± 6.3	17.9
(S)–I	−7.1 ± 5.5	2.8
(R)-I	−40.6 ± 19.1	16.1
(S)–V	−26.1 ± 5.3	10.4
(R)-V	−36.3 ± 7.1	14.4
(S)-VI	−15.8 ± 6.4	6.3
(R)-VI	−2.1 ± 4.5	0.8
VII	−27.0 ± 5.4	10.7
X	−37.3 ± 4.4	14.8

the piperidine varies, whereas the thiophene tail and other parts of the molecule remain identical in the binding pocket. Indeed, a shift of the piperidine ring away from His231 makes the (*S*)-enantiomer lose a π-cation interaction t© is present in **(*R*)-V** (Fig. S4C and D), and this is evident in the RMSD plot, where **R–V** is more stable compared to **S–V** (Fig. S5E and F). In line with this observation, **(*R*)-V** has a 1.4 times greater binding affinity relative to **(*S*)–V** (Table 5). In the case of **(*R*)-VI**, the quinoline moiety interacts with the loop Glu234 via an acceptor H-bond and π-π interactions with Tyr108 and His231, while the oxadiazole tail remains solvent-exposed without establishing any interaction (Fig. 4A–C). In the case of the **(*S*)-VI** enantiomer, the quinoline moiety moved in between Arg96 and Arg322 and interacted as a H-bond acceptor with the side chains of both residues, while the oxadiazole tail moved closer to His231 and interacted through the π-π interactions with His231, enhancing the stability of the tail in the binding pocket (Fig. 4B and C). The apparent better accommodation of **(*S*)-VI** compared to **(*R*)-VI** is reflected in the more than 7 times higher binding affinity of **(*S*)-VI** over **(*R*)-VI** in MD-based calculations (Table 5). Thus, the binding mode of VI at the FTO catalytic site in this study is supported by docking, MM-GBSA calculations, and long-timescale MD simulations. We acknowledge that orthogonal biophysical validation of this interaction (e.g., by thermal shift or SPR assays) would further strengthen the proposed model and will address this point in future hit-to-lead optimization studies. Nevertheless, the combination of enzymatic inhibition, selectivity over ALKBH5, cellular neuroprotection, favorable *in vitro* ADME properties, and *in vivo* efficacy provides a solid basis to consider VI a promising CNS-oriented FTO inhibitor hit.

3.7. DMPK profiling of selected novel FTO inhibitors

To characterize the *in vitro* safety and plasma stability of the selected FTO inhibitors, we evaluated their effects on hERG current at 10 μM and their persistence in mouse and human plasma over time. Studies revealed a differentiated profile among the FTO inhibitor hits. At 10 μM, compounds **I**, **V**, and **VI** showed a remaining hERG current of approximately 30–35% of control, whereas compounds **VII** and **X** reduced the current to below 10%, indicating a substantially higher hERG liability for the latter. FB23 exhibited an intermediate hERG inhibition profile within this concentration range. Plasma stability was high for all compounds, with residual fractions of 90–100% after incubation, indicating minimal degradation over the assay period. Solubility was also determined and found to be above 75 μM for all compounds tested (Table 6). Notably, compound **VI** combined an intermediate hERG liability, with robust plasma stability, supporting its selection as the preferred CNS-oriented lead among the tested hits (see Table 7).

3.8. Neuroprotective activity against Aβ toxicity

Differentiated SH-SY5Y cells were first preincubated with FTO inhibitors at various concentrations for 30 min. The medium was then

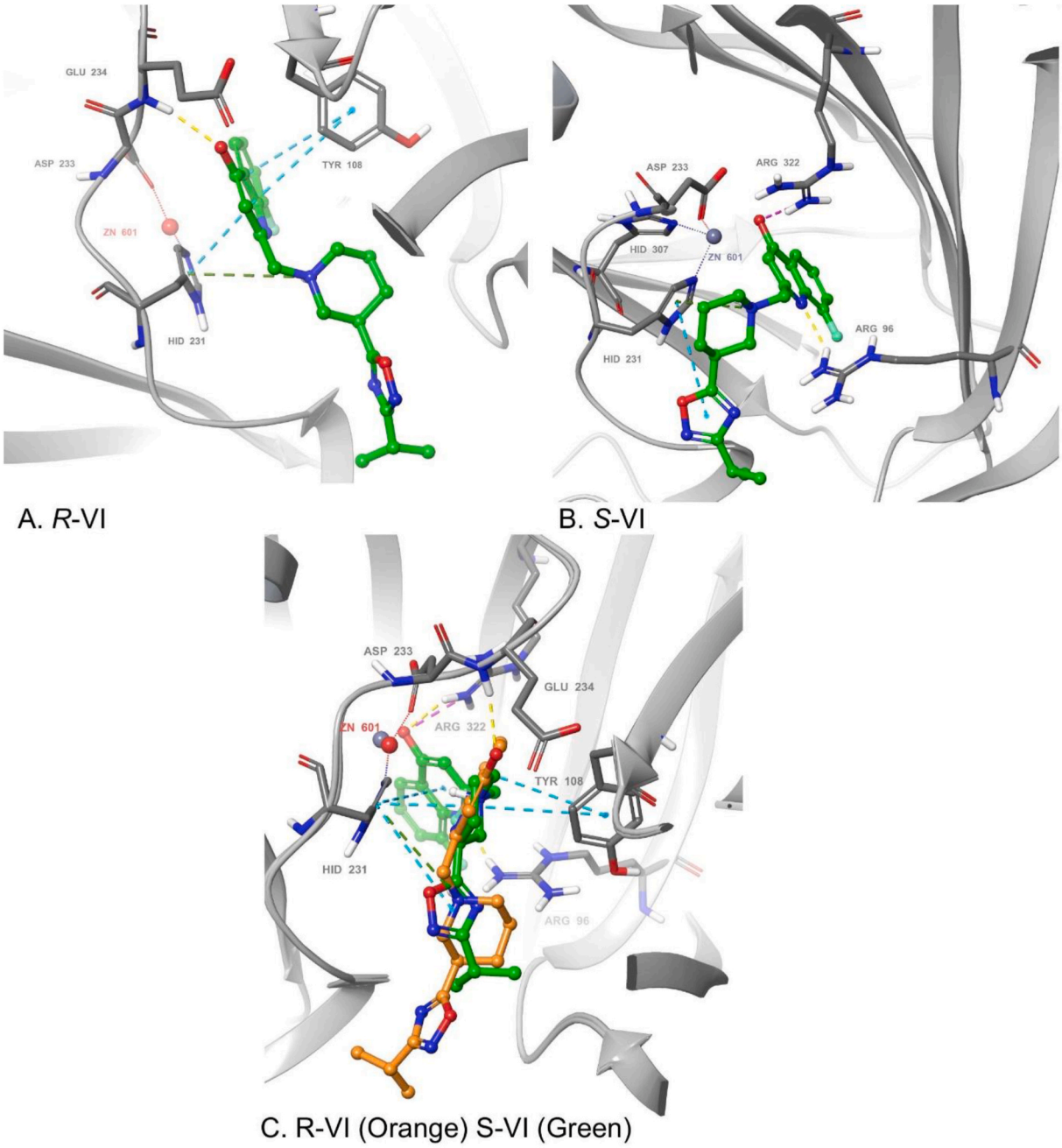


Fig. 4. 3D interactions of (**A**) (*R*) and (**B**) (*S*) enantiomers of **VI** within the substrate binding pocket ©FTO. (**C**) The binding pose of the (*R*) and (*S*) enantiomers of **VI** superimposed on each other in the substrate binding pocket of FTO.

replaced with fresh medium containing the same inhibitor concentrations and 5 μM Aβ (1-42) for an additional 24 h. Cell survival was quantified using the LDH release assay. Compounds **I**, **V**, **VI**, **VII**, and **X** were tested at concentrations from 0.001 to 50 μM, whereas FB23 was tested from 0.1 to 10 μM. Triton X-100 (4%) served as a positive control for complete cell death (Fig. 5).

As expected, exposure to Aβ (1-42) alone resulted in substantial neuronal cell death, reducing viability to approximately 30–40% of that in vehicle control (100% viability). Treatment with Triton X-100 (4%) confirmed complete cell lysis, validating assay performance. All tested FTO inhibitors significantly increased cell survival to >50% viability compared to Aβ-treated cultures, demonstrating statistically significant neuroprotection at 1 μM, a concentration selected based on the calculated IC_{50} values for each compound (Fig. 5A). At this range of concentration, compounds **I**, **V**, and **VI** achieved maximal protection (approximately 75–80% viability), slightly higher than that shown by the reference FB23 (65% viability), while compound **VII** exhibited slightly reduced but significant protection (~65–70% viability), and **X** did not elicit any protective effect (Fig. 5A).

Concentration-response analysis revealed that all five FTO inhibitor hits (**I**, **V**, **VI**, **VII**, and **X**) demonstrated dose-dependent neuroprotective activity. At low concentrations, cell viability remained substantially attenuated, approaching Aβ-induced toxicity levels. Within the overlapping concentration range tested for both FB23 and the newly identified hits (0.1–10 μM), compounds **I** and **VI** plateaued at approximately 70–85%, tended to afford equal or greater neuroprotection against Aβ-induced toxicity than FB23, which showed declined cell viability from approximately 75% at 0.1 μM to 65% at 1 μM, further declining to minimal protection (~50% survival) at 10 μM (Fig. 5B and C). At 50 μM, only the hit compounds were evaluated, and produced a sharp decline in

Table 6
Summary of experimental ADME assessment of selected novel FTO inhibitors.

Compound		hERG	Plasma stability (%)	Solubility (μM)
		Remaining current at 10 μM (% control)	t(360min)	
FB23	*Mouse*	24 ± 1	96.6	99.6
	Human		97.5	
I	*Mouse*	34 ± 3	101.4	>100
	Human		90.1	
V	*Mouse*	32 ± 5	99.9	95.5
	Human		98.5	
VI	*Mouse*	32 ± 6	100.5	75.6
	Human		98.4	
VII	*Mouse*	9 ± 4	89.1	94.6
	Human		102.9	
X	*Mouse*	6 ± 1	102.1	79.1
	Human		99.6	

viability to near-zero levels, indicating concentration-dependent toxicity at the highest dose tested (Fig. 5C). Thus, our comparison is restricted to the shared concentration range, establishing it as an optimal protective window with sustained efficacy, although a fully symmetrical dose–response analysis for all inhibitors will be required in future studies.

Collectively, these findings demonstrate that FTO inhibition confers moderate yet statistically significant protection against Aβ-induced neuronal cell death over 24 h, with hit compound **VI** displaying superior and more sustained neuroprotective profile compared to the reference compound FB23 across the therapeutically relevant dose range.

To further confirm target engagement at the RNA level, global m6A methylation was quantified in differentiated Aβ-treated SH-SY5Y cells (Fig. 5D). Treatment with compound **VI** at 1 μM produced a significant increase in m6A levels compared with Aβ-treated control cells, consistent with inhibition of the demethylase activity of FTO and with the observed neuroprotective effects. Notably, this increase in m6A methylation was associated with a significant downregulation of key pro-inflammatory genes, including *CXCL10*, *TNF-α*, and *HMOX1* (Fig. 5E, F, G, respectively). Given the central role of neuroinflammation in the pathogenesis of Aβ-induced neuronal damage, enhanced m6A methylation may contribute to the post-transcriptional regulation of transcripts involved in inflammatory pathways, thereby limiting the effects of sustained inflammatory signaling.

3.9. *In vivo* pharmacokinetic profile of selected FTO inhibitors

In vivo pharmacokinetic studies were carried out to assess the systemic exposure and CNS penetration following an intraperitoneal injection of a 3 mg/kg dose of FB23 and **VII**, and an oral administration of compound **VI** to the same dose in mice. Compound **VI** was evaluated by oral administration as it represents our hit candidate for anti-Alzheimer's therapeutic development, where oral bioavailability is essential for clinical translation and patient compliance in chronic treatment paradigms. Plasma concentration-time profiles over 24 h were analyzed, and brain tissue concentrations were measured to evaluate their potential for neurotherapeutic applications.

The reference FTO inhibitor FB23 reached the highest plasma concentration, with a C_{max} of 3286.7 ± 820.2 ng/mL at 5 min and maintained levels between 1000 and 2000 ng/mL for 240 min. Detectable levels lasted for over 20 h (Fig. 6A). Despite its favorable pharmacokinetic profile and plasma stability, FB23 was not detected in the brain, indicating no correlation between systemic exposure and its ability to cross the blood-brain barrier. Remarkably, FB23 was intentionally chosen as the reference inhibitor in this study because it is the most potent and widely used FTO inhibitor reported to date (IC_{50} = 0.06 μM). Our pharmacokinetic data show that, despite high and sustained plasma levels, FB23 remains undetectable in brain tissue under our experimental conditions, suggesting it does not cross the blood-brain barrier (BBB). In contrast, compound **VI** achieves oral brain exposure (Kp,brain = 0.58) and enhances cognition in SAMP8 mice. Therefore, our *in vivo* design aims to demonstrate the advantage of combining FTO inhibition with effective BBB penetration by comparing a potent but BBB-impermeant reference compound with a newly discovered, brain-penetrant chemotype. FB23-2, a hydroxamic acid derivative of FB23 with lower biochemical potency (IC_{50} = 2.6 μM) and improved cellular activity, is mentioned for context. It has been reported to exhibit brain exposure at higher doses. However, its hydroxamic scaffold may be linked to toxicity, and using an already brain-penetrant reference would weaken the intended comparison between the absence and presence of BBB permeability in this study.

Compound **VII** demonstrated rapid plasma exposure, reaching a C_{max} of 1075.2 ± 336.0 ng/mL within the first 5 min. However, it was cleared very quickly, maintaining very low plasmatic levels up to 20 h (Fig. 6B). Although the *in vitro* PAMPA-BBB assay predicted favorable CNS penetration, the *in vivo* PK study showed that compound **VII** did not reach the brain, suggesting that, despite its high initial plasma levels, further optimization is needed to improve its metabolic stability and BBB penetration.

Finally, the validated hit **VI** showed a favorable pharmacokinetic profile in both systemic and brain analyses after oral administration. Plasma C_{max} was 51.3 ± 9.8 ng/mL at 5 min, then declined bi-exponentially with residual levels detectable up to 4 h (Fig. 6C). Brain C_{max} was 29.9 ± 9.9 ng/g at a T_{max} of 5 min (Fig. 6D), with a Kp, brain of 0.58, indicating moderate *in vivo* CNS penetration consistent with the *in vitro* PAMPA-BBB data (Fig. 6E). It was also detected in cerebrospinal fluid (CSF), with a C_{max} of 5.71 ng/mL at 5 min (Fig. S6). Importantly, in our single-dose PK study, oral administration of compound **VI** at 3 mg/kg resulted in a maximum brain concentration of about 0.11 μM (C_{max}, brain ≈30 ng/g), which lies within one order of magnitude of its *in vitro* FTO inhibitory potency (IC_{50} = 1.1 μM). This level of brain exposure, together with the observed CNS target engagement under our dosing regimen, supports effective FTO inhibition at pharmacologically relevant concentrations. However, brain concentrations and Kp,uu,brain were not measured after chronic treatment in SAMP8 mice, representing a limitation of the study. Future research will include dedicated PK/PD studies to measure steady-state brain levels using the same strain and dosing schedule as in the behavioral tests. Overall, only compound **VI** showed sufficient PAMPA-BBB permeability (CNS+) and confirmed *in vivo* brain penetration, making it a promising hit for CNS-targeted FTO therapies, suitable for future hit-to-lead optimization.

Table 7
Summary of pharmacokinetic parameters of FTO inhibitors following a 3 mg/kg dose administration.

Compound	C_{max}, plasma (ng/mL)	T_{max}, plasma (min)	C_{max}, brain (ng/g)	T_{max}, brain (min)	Kp,brain	BBB Assessment
FB23	3286.7 ± 820.2	5	Not found	—	—	Non-Brain penetrant
VII	1075.2 ± 336.0	5	Not found	—	—	Non-Brain penetrant
VI	51.3 ± 9.8	5	29.9 ± 9.9	5	0.58	Brain penetrant

Values are shown as mean ± SEM (n = 2-3 mice per time point). C_{max} indicates the maximum concentration; T_{max} is the time to reach this maximum; Kp,brain is the brain-to-plasma partition coefficient at T_{max}. Brain tissue assessment showed undetectable levels of FB23 and **VII**.

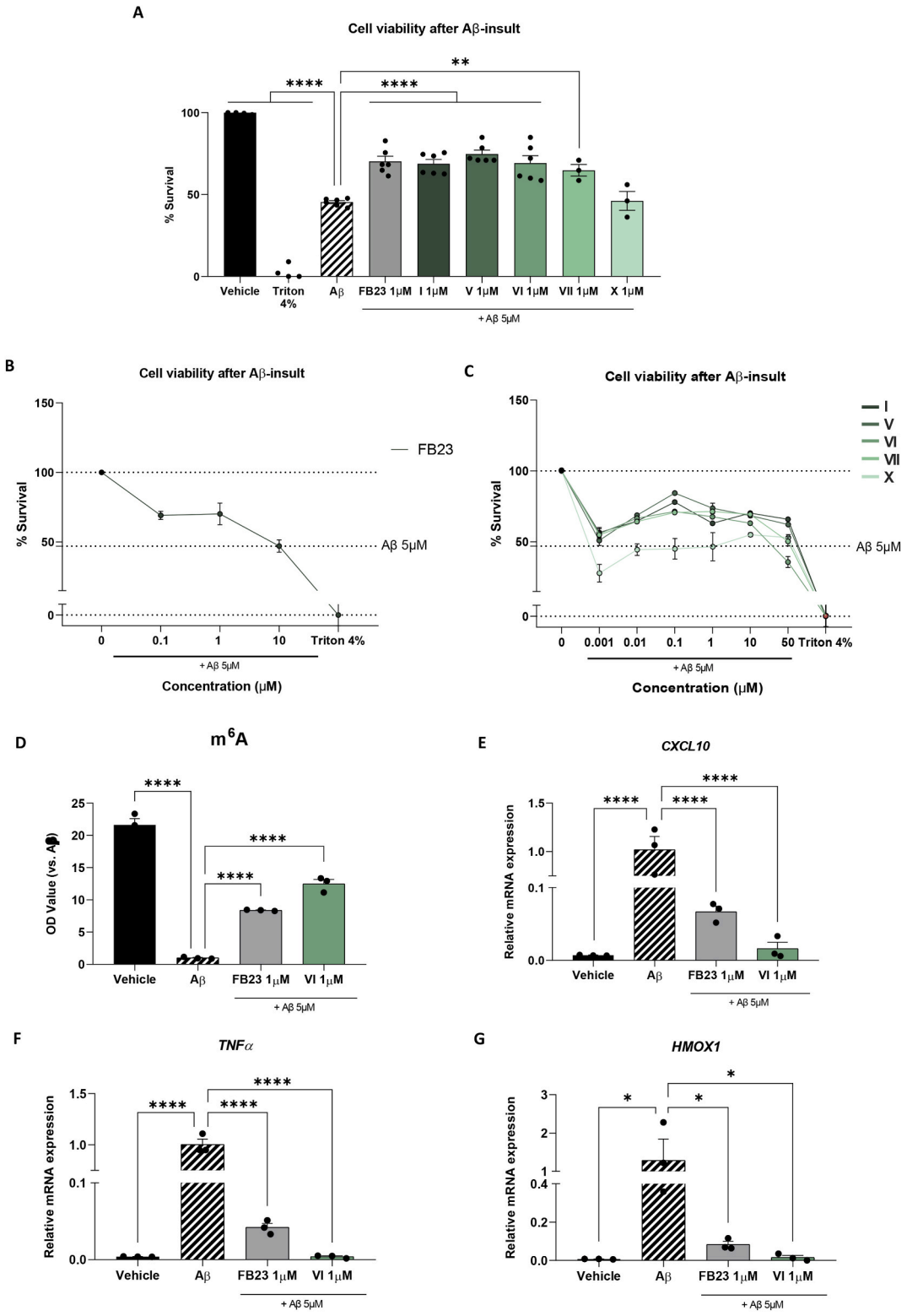


Fig. 5. Assessment of cell viability for novel FTO inhibitors. (**A**) All compounds at 1 μM. (**B**) Dose-response profile for FB23, and (**C**) our FTO inhibitor hits. Cells were treated with increasing concentrations of each compound (0.001 μM to 50 μM) for 24 h, and cell viability was measured using the LDH assay. Triton X-100 (4%) was used as a positive control for complete cell death. Results are expressed as a percentage of cell survival relative to vehicle-treated controls (0 μM = 100% survival). Data points represent mean ± SEM (n = 3 independent experiments with at least triplicate wells per condition). The horizontal reference line represents the survival of cells treated with Aβ alone (5 μM) in the absence of any inhibitor, serving as the baseline toxicity level against which compound-mediated protection is evaluated. (**D**) Quantification of m6A RNA methylation levels after Aβ-insult in FB23 1 μM and **VI** 1 μM groups. OD values were determined using the EpiQuik™ m6A RNA methylation Quantification Kit. Representative gene expression in the same groups of (**E**) *CXCL10*, (**F**) *TNFα* and (**G**) *HMOX1*. Relative mRNA expression levels were determined by real-time PCR. Values are expressed as mean ± SEM. +Aβ 5 μM indicates co-treatment with amyloid-β peptide where applicable. Statistical analysis: one-way ANOVA followed by Dunnett's post hoc analysis. *p < 0.05; **p < 0.01; ****p < 0.0001 (n ≥ 3).

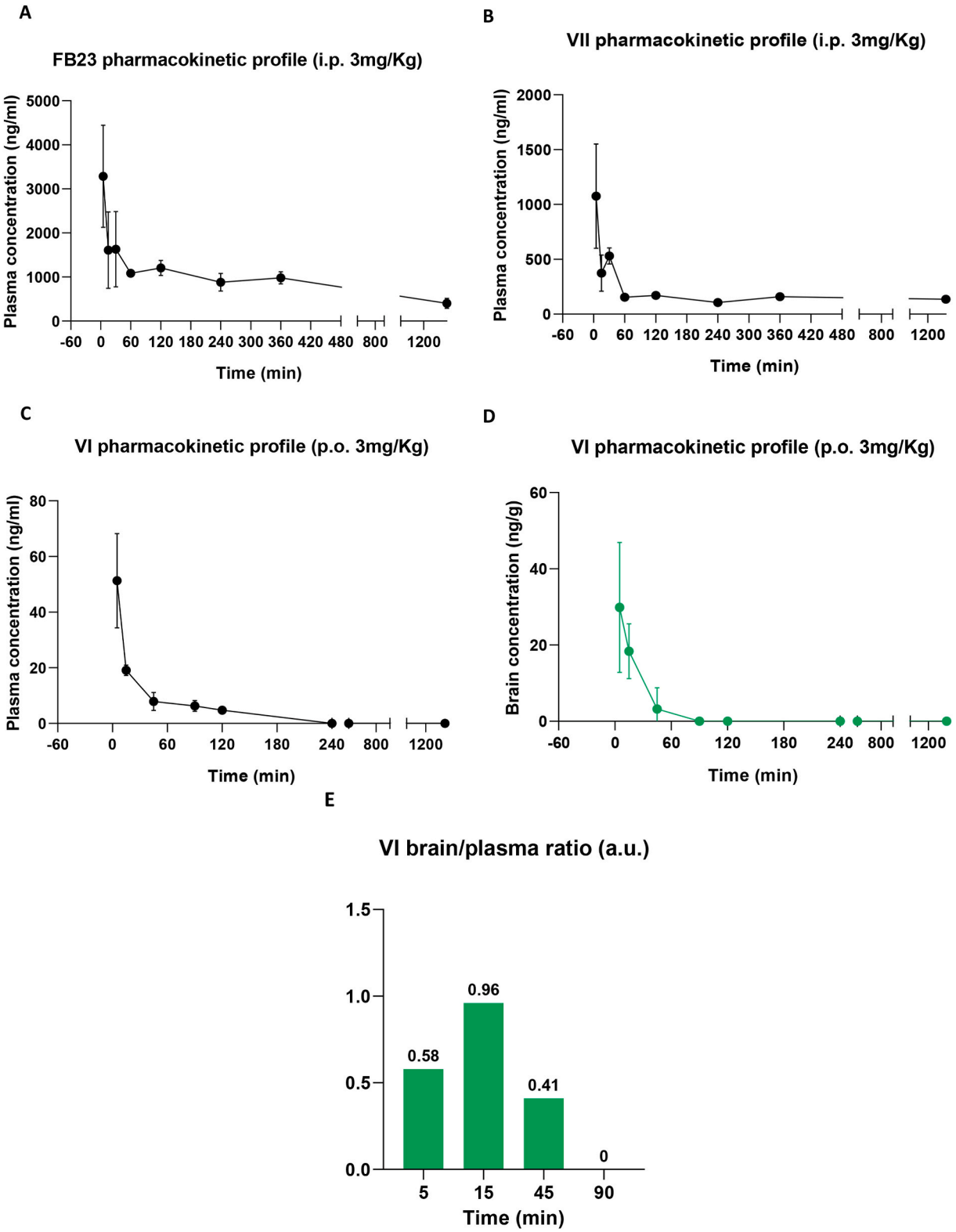


Fig. 6. Plasma and brain pharmacokinetic profiles of the validated FTO inhibitor hits **VI** and **VII** and the reference inhibitor FB23 following a 3 mg/kg dose administration. Concentration-time curves over 24 h in mice. (**A**) Plasma concentrations of FB23 demonstrated sustained systemic exposure with extended detection beyond 20 h. (**B**) Plasma concentrations of **VII** exhibit high C_{max} but rapid clearance. (**C-D**) Plasma and brain concentrations of **VI** show lower C_{max} with moderate CNS penetration. (**E**) Brain/plasma ratio of **VI** showing rapid initial brain penetration. Data points represent mean ± SEM (n = 2-3 mice per time point).

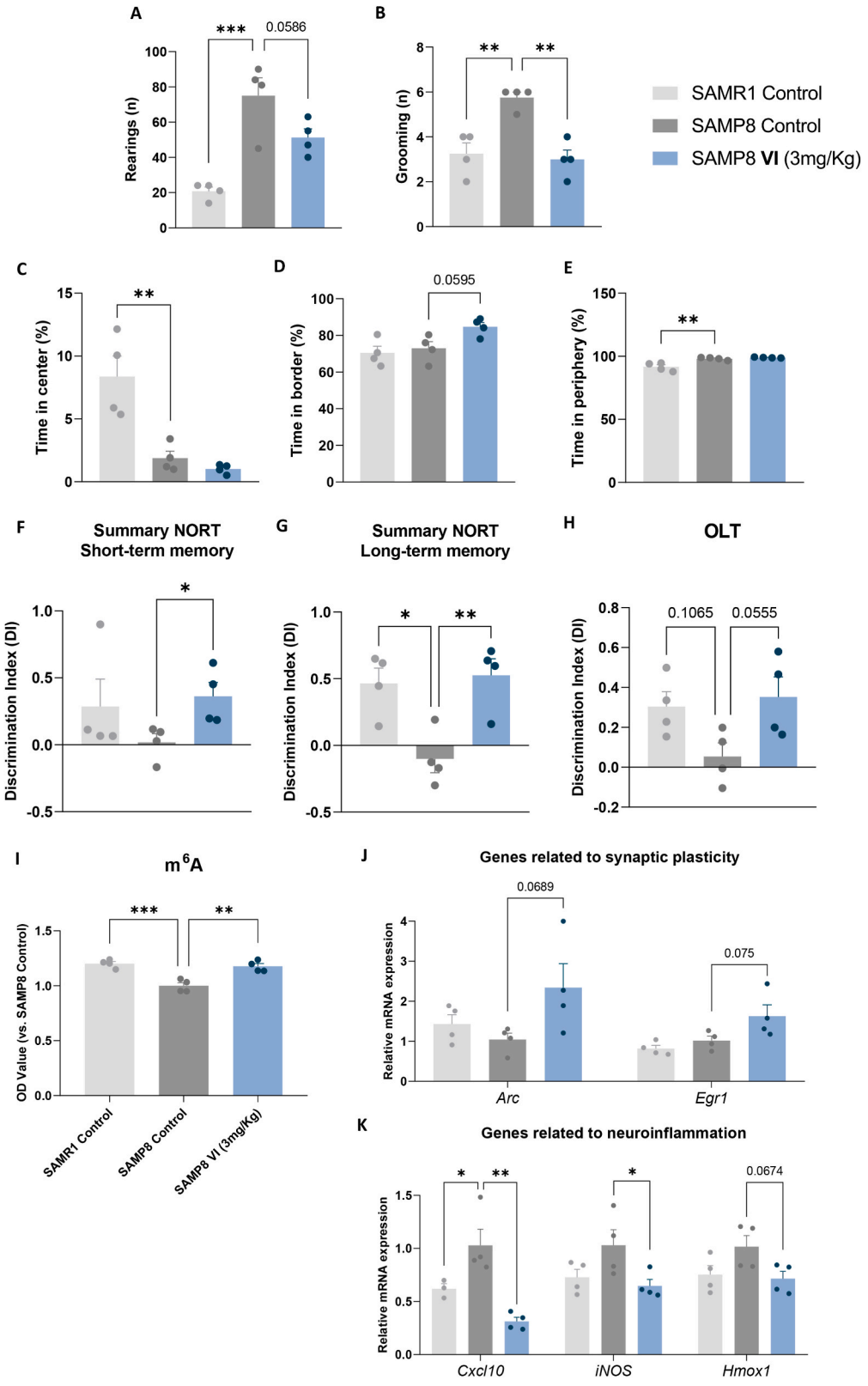


Fig. 7. Rescued cognitive deficits in SAMP8 mice after **VI** (3 mg/kg) oral treatment. The number of rearing (**A**) and grooming (**B**), and time spent in the center (**C**), border (**D**), and periphery (**E**) expressed as a percentage was measured by OFT. (**F**) Short-term and (**G**) long-term memory tests by NORT after 2 h and 24 h, respectively. (**H**) Spatial memory analysis by OLT. (**F–H**) Results are expressed as a discrimination index (DI). (**I**) Quantification of m6A RNA methylation levels in the brain. OD values were determined using the EpiQuik™ m6A RNA methylation Quantification Kit. Representative gene expression of (**J**) genes related to synaptic plasticity, including *Arc* and *Egr1,* and (**K**) genes related to neuroinflammation, including *Cxcl10*, *iNOS,* and *Hmox1*. Relative mRNA expression levels were determined by real-time PCR. Values are given as mean ± SEM. Statistical analysis: one-way ANOVA followed by Dunnett's post hoc analysis. *$p < 0.05$; **$p < 0.01$; ***$p < 0.001$ ($n = 4$).

3.10. Compound VI ameliorates cognitive deficits in SAMP8 mice

Chronic oral administration of compound VI (3 mg/kg, once daily for 4 weeks) significantly ameliorated cognitive deficits in SAMP8 mice [44]. Strikingly, OFT showed a significant decrease in **VI**-treated SAMP8 mice in both rearing and grooming (Fig. 7A and B), indicating an amelioration of anxiety-like behavior. Besides, SAMP8 Control mice demonstrated a significant decrease in time spent in the center compared to the SAMR1 Control group, as well as an increase in time spent in the periphery (Fig. 7C–E). Importantly, the SAMP8 **VI**-treated group showed an increasing tendency in time spent at the border compared to the SAMP8 Control mice (Fig. 7D).

Regarding NORT, SAMP8 Control mice exhibited deficits in both short- and long-term recognition memory, as reflected by a reduced preference for the novel object compared to SAMR1 controls. Treatment with compound **VI** significantly increased the discrimination index at both tests, indicating broad improvements in novel object recognition memory (Fig. 7F and G). Likewise, spatial memory was studied by OLT. As expected, SAMP8 control mice displayed a marked reduction in the discrimination index compared to the SAMR1 Control group, consistent with the characteristic impairment of hippocampal-dependent spatial memory observed in this strain. Notably, **VI**-treated SAMP8 mice showed a robust recovery of the discrimination index, reaching values comparable to those of SAMR1 mice, thereby demonstrating a clear rescue of spatial memory performance (Fig. 7H).

At the molecular level, target validation was consistent with the *in vitro* findings. **VI**-treated SAMP8 mice demonstrated significantly higher global m6A methylation levels in the brain compared to SAMP8 Control mice (Fig. 7I). In parallel, compound **VI** enhanced the expression of synaptic plasticity-associated immediate early genes, such as *Arc* and *Egr1,* which showed a clear increase (Fig. 7J), and diminished neuroinflammation, including *Cxcl10, iNOS,* and *Hmox1*, which showed a significant decrease (Fig. 7K). Together, these data indicate that compound **VI** exerts disease-modifying activity in SAMP8 mice, linking FTO inhibition and m6A remodeling to the rescue of cognitive and molecular deficits, thereby reinforcing its potential as a CNS-penetrant neurotherapeutic candidate for neurodegenerative conditions.

4. Conclusions

Through a combination of structure-based virtual screening, *in vitro* permeability and enzymatic assays, molecular dynamics simulations, neuroprotection studies, *in vivo* pharmacokinetic tests, and behavioral assessments in a senescence-accelerated mouse model, we identified compound **VI** as a highly promising FTO inhibitor for CNS use. **VI** shows low micromolar potency against human FTO, excellent selectivity over ALKBH5, and a strong neuroprotective effect against Aβ-induced toxicity in differentiated SH-SY5Y cells. Importantly, after oral dosing, **VI** reaches measurable plasma levels, exhibits moderate and consistent brain penetration (Kp, brain ≈0.60), and is detectable in CSF, meeting essential criteria for CNS drug development. In addition to these pharmacokinetic and cellular effects, long-term oral treatment with **VI** reduces age-related cognitive deficits in SAMP8 mice. It enhances hippocampal-dependent spatial and recognition memory and ameliorates anxiety-like behavior. This functional improvement in a well-established model of sporadic AD strongly indicates that selective FTO inhibition can modulate neurodegeneration-related cognitive decline *in vivo*.

On the other hand, although compound **VII** demonstrated good *in vitro* PAMPA-BBB permeability and micromolar FTO inhibition, its rapid systemic clearance and absence of detectable brain exposure *in vivo* emphasize the need for further optimization of its metabolic stability and CNS-related ADME properties. Similarly, FB23, despite its high potency and sustained systemic presence, did not significantly cross the BBB, which limits its potential for direct translation into neurological treatments.

Additionally, compound **VI** features a stereocenter and was tested as a racemic mixture in this study. Although resolving and analyzing each enantiomer separately would be scientifically valuable, it is beyond the scope of this initial hit-discovery phase and will be addressed during subsequent hit-to-lead development. Importantly, all *in vivo* data shown here were obtained using the racemate and consistently support **VI** as a promising CNS-targeted FTO inhibitor candidate. Our results emphasize that developing effective FTO inhibitors for CNS disorders requires balancing enzymatic potency, selectivity, BBB permeability, cellular activity, pharmacokinetics, and *in vivo* efficacy in relevant disease models. In this comprehensive optimization, compound **VI** emerges as a promising candidate for further medicinal chemistry modifications and mechanistic studies in models of FTO-related cognitive decline and neurodegeneration. This strategy underpins the rational design of next-generation epitranscriptomic modulators with potential to alter disease progression in AD and similar dementias (Fig. S7).

Funding

This study was supported by the Ministerio de Ciencia, Innovación y Universidades (MICIU), Agencia Estatal de Investigación (AEI), and European Union NextGenerationEU/PRTR (PID2022-139016OA-I00, PDC2022-133441-I00: to CGF and MP; PID2023-147004OB-I00: to DM-T and AM-A), Generalitat de Catalunya (2021 SGR 00357: to CGF, MP, and DM-T), Xunta de Galicia (ED431C 2022/20 to JB) and European Regional Development Fund (ERDF to JB). This study was co-financed by Secretaria d'Universitats i Recerca del Departament d'Empresa i Coneixement de la Generalitat de Catalunya 2022 (Producte 0092; Llavor 005 and 007; to CGF). AI acknowledges the Agència de Gestió d'Ajuts Universitaris i de Recerca (AGAUR) for her FI Joan Oró predoctoral fellowship (2023 FI-1 00944). ABS acknowledges the financial support of Càtedra UB Dr. Antoni Esteve i Subirana de Recerca en Farmacologia.

CRediT authorship contribution statement

Alba Irisarri: Formal analysis, Investigation, Methodology, Visualization, Writing – original draft. **Aina Bellver-Sanchis:** Investigation, Methodology, Writing – original draft. **Bhanwar Singh Choudhary:** Conceptualization, Writing – original draft. **Ana Mallo-Abreu:** Formal analysis, Visualization, Writing – original draft. **Luis Labrador:** Investigation, Methodology. **Gemma Casadesus:** Methodology, Visualization. **Belén Pérez:** Data curation, Methodology. **Abhisek Jana:** Investigation, Methodology. **Deb Ranjan Banerjee:** Investigation, Methodology, Writing – original draft. **Isabel Iriepa:** Investigation, Methodology, Writing – original draft. **M. Isabel Loza:** Investigation, Methodology. **José Brea:** Investigation, Methodology. **Cristina Val:** Investigation, Methodology. **Mercè Pallàs:** Conceptualization, Writing – original draft. **Diego Muñoz-Torrero:** Investigation, Supervision, Writing – original draft. **Christian Griñán-Ferré:** Conceptualization, Data curation, Formal analysis, Supervision, Validation, Visualization, Writing – original draft, Writing – review & editing.

Declaration of competing interest

The authors declare that they have no known competing financial interests or personal relationships that could have appeared to influence the work reported in this paper.

Appendix A. Supplementary data

Supplementary data to this article can be found online at https://doi.org/10.1016/j.ejmech.2026.118852.

Data availability

Data will be made available on request.

References

[1] P.C. He, C. He, m 6 A RNA methylation: from mechanisms to therapeutic potential, EMBO J. 40 (2021) e105977, https://doi.org/10.15252/embj.2020105977.

[2] Z. Gao, X. Zha, M. Li, X. Xia, S. Wang, Insights into the m6A demethylases FTO and ALKBH5 : structural, biological function, and inhibitor development, Cell Biosci. 14 (2024) 108, https://doi.org/10.1186/s13578-024-01286-6.

[3] G. Jia, Y. Fu, X. Zhao, Q. Dai, G. Zheng, Y. Yang, C. Yi, T. Lindahl, T. Pan, Y. G. Yang, C. He, N6-Methyladenosine in nuclear RNA is a major substrate of the obesity-associated FTO, Nat. Chem. Biol. 7 (2011) 885–887, https://doi.org/10.1038/nchembio.687.

[4] J. Wei, F. Liu, Z. Lu, Q. Fei, Y. Ai, P.C. He, H. Shi, X. Cui, R. Su, A. Klungland, G. Jia, J. Chen, C. He, Differential m 6 A, m 6 A m , and m 1 A demethylation mediated by FTO in the cell nucleus and cytoplasm, Mol. Cell 71 (2018) 973–985.e5, https://doi.org/10.1016/j.molcel.2018.08.011.

[5] S. Huff, I.R. Kummetha, L. Zhang, L. Wang, W. Bray, J. Yin, V. Kelley, Y. Wang, T. M. Rana, Rational design and optimization of m6A-RNA demethylase FTO inhibitors as anticancer agents, J. Med. Chem. 65 (2022) 10920–10937, https://doi.org/10.1021/acs.jmedchem.1c02075.

[6] A.M. Angelidi, M.J. Belanger, A. Kokkinos, C.C. Koliaki, C.S. Mantzoros, Novel noninvasive approaches to the treatment of obesity: from pharmacotherapy to gene therapy, Endocr. Rev. 43 (2022) 507–557, https://doi.org/10.1210/endrev/bnab034.

[7] S.K. Azzam, H. Alsafar, A.A. Sajini, FTO m6A demethylase in obesity and cancer: implications and underlying molecular mechanisms, Int. J. Mol. Sci. 23 (2022) 3800, https://doi.org/10.3390/ijms23073800.

[8] C. Ren, Z. Cao, Y. Liu, R. Wang, C. Lin, Z. Wang, Medicinal chemistry aspects of fat mass and obesity associated protein: structure, function and inhibitors, Future Med. Chem. 16 (2024) 1705–1726, https://doi.org/10.1080/17568919.2024.2380245.

[9] R. Su, L. Dong, Y. Li, M. Gao, L. Han, M. Wunderlich, X. Deng, H. Li, Y. Huang, L. Gao, C. Li, Z. Zhao, S. Robinson, B. Tan, Y. Qing, X. Qin, E. Prince, J. Xie, H. Qin, W. Li, C. Shen, J. Sun, P. Kulkarni, H. Weng, H. Huang, Z. Chen, B. Zhang, X. Wu, M.J. Olsen, M. Müschen, G. Marcucci, R. Salgia, L. Li, A.T. Fathi, Z. Li, J.C. Mulloy, M. Wei, D. Horne, J. Chen, Targeting FTO suppresses cancer stem cell maintenance and immune evasion, Cancer Cell 38 (2020) 79–96.e11, https://doi.org/10.1016/j.ccell.2020.04.017.

[10] J. Zhang, G. Li, R. Wu, L. Shi, C. Tian, H. Jiang, H. Che, Y. Jiang, Z. Jin, R. Yu, X. Liu, X. Zhang, The m6A RNA demethylase FTO promotes radioresistance and stemness maintenance of glioma stem cells, Cell. Signal. 132 (2025) 111782, https://doi.org/10.1016/j.cellsig.2025.111782.

[11] L. Ji, L. Pu, J. Wang, H. Cao, S. Melemenidis, S. Sinha, L. Guan, E.E. Laseinde, R. von Eyben, S.A. Richter, J.M. Nam, C. Kong, K.M. Casey, E.E. Graves, R.L. Frock, Q.T. Le, E.B. Rankin, FTO inhibition enhances the therapeutic index of radiation therapy in head and neck cancer, JCI Insight 10 (2025) e184968, https://doi.org/10.1172/jci.insight.184968.

[12] L. Jiang, R. Liang, Q. Luo, Z. Chen, G. Song, Targeting FTO suppresses hepatocellular carcinoma by inhibiting ERBB3 and TUBB4A expression, Biochem. Pharmacol. 226 (2024), https://doi.org/10.1016/j.bcp.2024.116375.

[13] L. Prabhakar, D.J.G. Davis, Computational study of potential inhibitors for fat mass and obesity-associated protein from seaweed and plant compounds, PeerJ 10 (2022) e14256, https://doi.org/10.7717/peerj.14256.

[14] Y. Huang, W. Xia, Z. Dong, C.G. Yang, Chemical inhibitors targeting the oncogenic m6A modifying proteins, Acc. Chem. Res. 56 (2023) 3010–3022, https://doi.org/10.1021/acs.accounts.3c00451.

[15] Y. Wang, X. Li, M. Liu, X. Xu, Y. Ma, Y. Luo, Y. Wang, N6-methyladenosine methylation: a novel key to unlocking mental disorders, Int. J. Neuropsychopharmacol. 28 (2025) pyaf044, https://doi.org/10.1093/ijnp/pyaf044.

[16] R. Chang, Z. Huang, S. Zhao, J. Zou, Y. Li, S. Tan, Emerging roles of FTO in neuropsychiatric disorders, BioMed Res. Int. 2022 (2022) 2677312, https://doi.org/10.1155/2022/2677312.

[17] H. Mitsuhashi, C. Nagy, Potential roles of m6A and FTO in synaptic connectivity and major depressive disorder, Int. J. Mol. Sci. 24 (2023) 6220, https://doi.org/10.3390/ijms24076220.

[18] J. Mathoux, D.C. Henshall, G.P. Brennan, Regulatory mechanisms of the RNA modification m6A and significance in brain function in health and disease, Front. Cell. Neurosci. 15 (2021) 671932, https://doi.org/10.3389/fncel.2021.671932.

[19] Y.P. Yen, J.A. Chen, The m6A epitranscriptome on neural development and degeneration, J. Biomed. Sci. 28 (2021) 40, https://doi.org/10.1186/s12929-021-00734-6.

[20] L. Xia, F. Zhang, Y. Li, Y. Mo, L. Zhang, Q. Li, M. Luo, X. Hou, Z. Du, J. Deng, E. Hao, A new perspective on Alzheimer's disease: m6A modification, Front. Genet. 14 (2023) 1166831, https://doi.org/10.3389/fgene.2023.1166831.

[21] S. Gao, Y. Wang, X. Li, Y. Liang, Z. Jin, B. Yang, T.F. Yuan, H. Tian, B. Peng, Y. Rao, Dynamics of N6-methyladenosine modification during Alzheimer's disease development, Heliyon 10 (2024) e26911, https://doi.org/10.1016/j.heliyon.2024.e26911.

[22] B. Hu, Y. Shi, F. Xiong, Y.T. Chen, X. Zhu, E. Carrillo, X. Wen, N. Drolet, C. S. Rajpurohit, X. Xu, D.F. Lee, C. Soto, S. Zhong, V. Jayaraman, H. Zheng, W. Li, Rewired m6A of promoter antisense RNAs in Alzheimer's disease regulates neuronal genes in 3D nucleome, Nat. Commun. 16 (2025) 1–20, https://doi.org/10.1038/s41467-025-60378-0.

[23] G. Xie, X.N. Wu, Y. Ling, Y. Rui, D. Wu, J. Zhou, J. Li, S. Lin, Q. Peng, Z. Li, H. Wang, H. Bin Luo, A novel inhibitor of N6-methyladenosine demethylase FTO induces mRNA methylation and shows anti-cancer activities, Acta Pharm. Sin. B 12 (2022) 853–866, https://doi.org/10.1016/j.apsb.2021.08.028.

[24] L. Zhang, J. Wei, Z. Zou, C. He, RNA modification systems as therapeutic targets, Nat. Rev. Drug Discov. 25 (2025) 59–78, https://doi.org/10.1038/s41573-025-01280-8.

[25] D. Greco, Z. Čočková, D. Das, A.S. Mali, J. Novotný, M.J. Olsen, P. Telenský, Small molecule FTO inhibitor MO-I-500 protects differentiated SH-SY5Y neuronal cells from oxidative stress, Front. Mol. Neurosci. 18 (2026) 1736173, https://doi.org/10.3389/fnmol.2025.1736173.

[26] Y. Huang, J. Yan, Q. Li, J. Li, S. Gong, H. Zhou, J. Gan, H. Jiang, G.F. Jia, C. Luo, C. G. Yang, Meclofenamic acid selectively inhibits FTO demethylation of m6A over ALKBH5, Nucleic Acids Res. 43 (2015) 373–384, https://doi.org/10.1093/nar/gku1276.

[27] S. Huff, S.K. Tiwari, G.M. Gonzalez, Y. Wang, T.M. Rana, M6A-RNA demethylase FTO inhibitors impair self-renewal in glioblastoma stem cells, ACS Chem. Biol. 16 (2021) 324–333, https://doi.org/10.1021/acschembio.0c00841.

[28] Y. Huang, R. Su, Y. Sheng, L. Dong, Z. Dong, H. Xu, T. Ni, Z.S. Zhang, T. Zhang, C. Li, L. Han, Z. Zhu, F. Lian, J. Wei, Q. Deng, Y. Wang, M. Wunderlich, Z. Gao, G. Pan, D. Zhong, H. Zhou, N. Zhang, J. Gan, H. Jiang, J.C. Mulloy, Z. Qian, J. Chen, C.G. Yang, Small-molecule targeting of oncogenic FTO demethylase in acute myeloid leukemia, Cancer Cell 35 (2019) 677–691.e10, https://doi.org/10.1016/j.ccell.2019.03.006.

[29] D. Ma, X. Liu, X. Zhang, Y. Hong, Y. Wang, F. Zhang, L. Du, J. Zhao, Q. Wang, C. Chang, W. Liu, Y. Lou, X. Liu, Discovery of the 2,3-Dihydrobenzopyrane-4-one as a potent FTO inhibitor against obesity-related metabolic diseases, J. Med. Chem. 68 (2025) 7421–7440, https://doi.org/10.1021/acs.jmedchem.4c03124.

[30] M. Prakash, Y. Itoh, Y. Fujiwara, Y. Takahashi, Y. Takada, P. Mellini, E.E. Elboray, M. Terao, Y. Yamashita, C. Yamamoto, T. Yamaguchi, M. Kotoku, Y. Kitao, R. Singh, R. Roy, S. Obika, M. Oba, D.O. Wang, T. Suzuki, Identification of potent and selective inhibitors of fat mass obesity-associated protein using a fragment-merging approach, J. Med. Chem. 64 (2021) 15810–15824, https://doi.org/10.1021/acs.jmedchem.1c01107.

[31] Z. Liu, Z. Duan, D. Zhang, P. Xiao, T. Zhang, H. Xu, C.H. Wang, G.W. Rao, J. Gan, Y. Huang, C.G. Yang, Z. Dong, Structure-activity relationships and antileukemia effects of the tricyclic benzoic acid FTO inhibitors, J. Med. Chem. 65 (2022) 10638–10654, https://doi.org/10.1021/acs.jmedchem.2c00848.

[32] T. Yang, Z. Dong, R. Du, Y. Wang, L. Liu, Y. Xue, X. Zhang, Y. Liao, J. Gan, X. Yu, Y. Huang, C.G. Yang, Development of orally bioavailable FTO inhibitors with potent antileukemia efficacy, J. Med. Chem. 68 (2025) 13714–13727, https://doi.org/10.1021/acs.jmedchem.5c00566.

[33] X. Zhang, Z. Wang, X. Xie, G. Liu, Z. Dong, C.G. Yang, Structure-based design of a highly potent dual-competitive FTO inhibitor for targeted m6A demethylase inhibition in AML, J. Med. Chem. 68 (2025) 22779–22798, https://doi.org/10.1021/acs.jmedchem.5c01738.

[34] L.L. Zhou, H. Xu, Y. Huang, C.G. Yang, Targeting the RNA demethylase FTO for cancer therapy, RSC Chem. Biol. 2 (2021) 1352–1369, https://doi.org/10.1039/d1cb00075f.

[35] W. Aik, M. Demetriades, M.K.K. Hamdan, E.A.L. Bagg, K.K. Yeoh, C. Lejeune, Z. Zhang, M.A. McDonough, C.J. Schofield, Structural basis for inhibition of the fat mass and obesity associated protein (FTO), J. Med. Chem. 56 (2013) 3680–3688, https://doi.org/10.1021/jm400193d.

[36] G. Madhavi Sastry, M. Adzhigirey, T. Day, R. Annabhimoju, W. Sherman, Protein and ligand preparation: parameters, protocols, and influence on virtual screening enrichments, J. Comput. Aided Mol. Des. 27 (2013) 221–234, https://doi.org/10.1007/s10822-013-9644-8.

[37] R.A. Friesner, J.L. Banks, R.B. Murphy, T.A. Halgren, J.J. Klicic, D.T. Mainz, M. P. Repasky, E.H. Knoll, M. Shelley, J.K. Perry, D.E. Shaw, P. Francis, P.S. Shenkin, Glide: a new approach for rapid, accurate docking and scoring. 1. Method and assessment of docking accuracy, J. Med. Chem. 47 (2004) 1739–1749, https://doi.org/10.1021/jm0306430.

[38] R.A. Friesner, R.B. Murphy, M.P. Repasky, L.L. Frye, J.R. Greenwood, T.A. Halgren, P.C. Sanschagrin, D.T. Mainz, Extra precision glide: docking and scoring incorporating a model of hydrophobic enclosure for protein-ligand complexes, J. Med. Chem. 49 (2006) 6177–6196, https://doi.org/10.1021/jm051256o.

[39] L. Di, E.H. Kerns, K. Fan, O.J. McConnell, G.T. Carter, High throughput artificial membrane permeability assay for blood-brain barrier, Eur. J. Med. Chem. 38 (2003) 223–232, https://doi.org/10.1016/S0223-5234(03)00012-6.

[40] B.R. Brooks, C.L. Brooks, A.D. Mackerell, L. Nilsson, R.J. Petrella, B. Roux, Y. Won, G. Archontis, C. Bartels, S. Boresch, A. Caflisch, L. Caves, Q. Cui, A.R. Dinner, M. Feig, S. Fischer, J. Gao, M. Hodoscek, W. Im, K. Kuczera, T. Lazaridis, J. Ma, V. Ovchinnikov, E. Paci, R.W. Pastor, C.B. Post, J.Z. Pu, M. Schaefer, B. Tidor, R. M. Venable, H.L. Woodcock, X. Wu, W. Yang, D.M. York, M. Karplus, CHARMM: the biomolecular simulation program, J. Comput. Chem. 30 (2009) 1545–1614, https://doi.org/10.1002/jcc.21287.

[41] K.J. Bowers, E. Chow, H. Xu, R.O. Dror, M.P. Eastwood, B.A. Gregersen, J. L. Klepeis, I. Kolossvary, M.A. Moraes, F.D. Sacerdoti, J.K. Salmon, Y. Shan, D. E. Shaw, Scalable algorithms for molecular dynamics simulations on commodity clusters, in: Proceedings of the 2006 ACM/IEEE Conference on Supercomputing, SC'06, 2006, https://doi.org/10.1145/1188455.1188544.

[42] B.R. Miller, T.D. McGee, J.M. Swails, N. Homeyer, H. Gohlke, A.E. Roitberg, MMPBSA.py: an efficient program for end-state free energy calculations, J. Chem. Theor. Comput. 8 (2012) 3314–3321, https://doi.org/10.1021/ct300418h.
[43] A.K. Ghose, T. Herbertz, R.L. Hudkins, B.D. Dorsey, J.P. Mallamo, Knowledge-based, central nervous system (CNS) lead selection and lead optimization for CNS drug discovery, ACS Chem. Neurosci. 3 (2012) 50–68, https://doi.org/10.1021/cn200100h.
[44] C. Griñán-Ferré, R. Corpas, D. Puigoriol-Illamola, V. Palomera-Ávalos, C. Sanfeliu, M. Pallàs, Understanding epigenetics in the neurodegeneration of Alzheimer's disease: SAMP8 mouse model, J. Alzheimers Dis. 62 (2018) 943–963, https://doi.org/10.3233/JAD-170664.